The Astrophysical Journal, 1002:99 (14pp), 2026 May 1 https://doi.org/10.3847/1538-4357/ae595e

Signature of a Magnetar Central Engine from the Multiband Afterglow of GRB 151027A Associated with a Supernova

Liang-Jun Chen[1,2], Xiang-Gao Wang[1,2], Hou-Jun Lü[1,2], WeiKang Zheng[3], Daniel A. Perley[4], Da-Bin Lin[1,2], Yihan Wang[5,6], De-Feng Kong[1,2], You-Dong Hu[1,2], Jie Xia[7,8], S. Bradley Cenko[9], Hong-Bang Liu[1,2], Fei Xie[1,2], Jing Lü[1,2], En-Wei Liang[1,2], Bing Zhang[10,11,12,13], and Alexei V. Filippenko[3]

[1] Guangxi Key Laboratory for Relativistic Astrophysics, School of Physical Science and Technology, Guangxi University, Nanning 530004, People's Republic of China; wangxg@gxu.edu.cn, lhj@gxu.edu.cn
[2] GXU-NAOC Center for Astrophysics and Space Sciences, Nanning 530004, People's Republic of China
[3] Department of Astronomy, University of California, Berkeley, CA 94720-3411, USA; weikang@berkeley.edu, afilippenko@berkeley.edu
[4] Astrophysics Research Institute, Liverpool John Moores University, 146 Brownlow Hill, Liverpool, L3 5RF, UK; d.a.perley@ljmu.ac.uk
[5] Department of Astronomy, University of Wisconsin, Madison, WI 53706, USA
[6] The Nevada Center for Astrophysics, University of Nevada, Las Vegas, NV 89102, USA
[7] Division of Dark Matter and Space Astronomy, Purple Mountain Observatory, Chinese Academy of Sciences, Nanjing 210023, People's Republic of China; xiajie@pmo.ac.cn
[8] School of Astronomy and Space Science, University of Science and Technology of China, Hefei 230026, People's Republic of China
[9] Astrophysics Science Division, NASA Goddard Space Flight Center, Mail Code 661, Greenbelt, MD 20771, USA
[10] The Hong Kong Institute for Astronomy and Astrophysics, University of Hong Kong, Pokfulam Road, Hong Kong, People's Republic of China
[11] Department of Physics, University of Hong Kong, Pokfulam Road, Hong Kong, People's Republic of China
[12] The Nevada Center for Astrophysics, University of Nevada, Las Vegas, NV 89154, USA
[13] Department of Physics and Astronomy, University of Nevada, Las Vegas, NV 89154, USA
Received 2025 December 29; revised 2026 March 17; accepted 2026 March 26; published 2026 April 28

Abstract

We report multiwavelength observations and theoretical modeling of the afterglow of gamma-ray burst (GRB) 151027A. The object exhibits a complete evolutionary sequence, including prompt gamma-ray and optical emission, an initial optical onset bump, an optical rebrightening, a late-time supernova bump, an X-ray flare, and two distinct X-ray plateaus. GRB 151027A exhibits nearly all characteristic features observed in GRB afterglows. Such a rich set of features within a single event is exceptionally rare. We show that the first X-ray plateau followed by a rapid decay can be attributed to the collapse of a newly formed magnetar to form a black hole. The second X-ray plateau can be explained by fallback accretion. We find that the energy-injection model successfully reproduces the optical rebrightening of GRB 151027A. The late-time optical bump is well described by a ^{56}Ni-powered supernova light curve. GRB 151027A presents a complete physical picture for GRB phenomenology, whereas reconstructing such a comprehensive picture previously required the statistical analysis of multiple GRBs.

Unified Astronomy Thesaurus concepts: Gamma-ray bursts (629); Magnetars (992); Supernovae (1668)

Materials only available in the online version of record: machine-readable tables

1. Introduction

Gamma-ray bursts (GRBs) are among the most energetic phenomena in the Universe, observed daily at random positions across the sky (e.g., R. W. Klebesadel et al. 1973; C. A. Meegan et al. 1992; P. Kumar & B. Zhang 2015; B. Zhang 2018). They are traditionally categorized into two distinct populations, based on the duration of their prompt gamma-ray emission (T_{90}): short-duration GRBs (SGRBs) and long-duration GRBs (LGRBs), with a crossover duration of 2 s (C. Kouveliotou et al. 1993). Here, T_{90} is defined as the time interval containing 90% of the total fluence from 5% to 95% accumulation. This phenomenological classification is strongly supported by their proposed progenitors. SGRBs are widely believed to originate from mergers of compact binary systems, such as two neutron stars or a neutron star and a black hole. This connection was confirmed by the coincident detection of gravitational waves and electromagnetic counterparts (a kilonova) from GW170817/GRB 170817A (B. P. Abbott et al. 2017; E. Pian et al. 2017; N. R. Tanvir et al. 2017; J. Ren et al. 2019). LGRBs are linked to the core collapse of massive stars, as evidenced by the frequent association with broad-lined type Ic supernovae (SNe; T. J. Galama et al. 1998; S. R. Kulkarni et al. 1998; J. Hjorth et al. 2003; K. Z. Stanek et al. 2003; S. E. Woosley & J. S. Bloom 2006; A. M. Soderberg 2007; J. Hjorth & J. S. Bloom 2012; H.-J. Lü et al. 2018a). In both scenarios, the catastrophic event is expected to lead to the formation of a central engine (a black hole or a magnetar; V. V. Usov 1992; S. E. Woosley 1993; C. Thompson 1994; Z. G. Dai & T. Lu 1998; W. Kluźniak & M. Ruderman 1998; R. Popham et al. 1999; H. K. Lee et al. 2000; R. Narayan et al. 2001; B. D. Metzger et al. 2011; S. Nagataki 2011; H.-J. Lü & B. Zhang 2014; X.-G. Wang et al. 2020). This newly formed central engine then launches ultrarelativistic, collimated outflows (jets). These outflows power prompt emission, brief and intense flashes of gamma rays known as GRBs, followed by longer-lived afterglow radiation that ranges from radio and optical to X-ray emission. In recent years, very-high-energy ($\gtrsim$100 GeV) gamma-ray afterglow emission has also been detected from some GRB afterglows (H. Abdalla et al. 2019;

MAGIC Collaboration 2019; H.E.S.S. Collaboration et al. 2021; LHAASO Collaboration et al. 2023; H. Abe et al. 2024).

The canonical X-ray afterglow light curve typically exhibits five distinct components (J. A. Nousek et al. 2006; B. Zhang et al. 2006): (1) an initial steep decay phase, which is the tail of the prompt emission, interpreted as the so-called curvature effect or high-latitude radiation (E. E. Fenimore et al. 1996; P. Kumar & A. Panaitescu 2000; G. Tagliaferri et al. 2005; E. W. Liang et al. 2006; J. A. Nousek et al. 2006; A. Panaitescu et al. 2006; R. Yamazaki et al. 2006; B. Zhang et al. 2006); (2) the shallow decay phase (or plateau), widely attributed to continuous energy injection into the external shock (Z. G. Dai & T. Lu 1998; M. J. Rees & P. Mészáros 1998; B. Zhang & P. Mészáros 2001a; E.-W. Liang et al. 2007); (3) the normal decay phase, which is expected in the standard forward-shock model (P. Mészáros & M. J. Rees 1997; R. Sari et al. 1998); (4) the late steepening phase (jet break), caused by the achromatic steepening when the jet slows down and its relativistic beaming angle exceeds the jet opening angle (J. E. Rhoads 1997, 1999; R. Sari et al. 1999); and (5) X-ray flares that are powered by late-time central engine activity (G. Chincarini et al. 2010).

Beyond the above components, optical afterglows display distinct additional features (L. Li et al. 2012): (1) prompt optical flares that track the gamma-ray emission (W. T. Vestrand et al. 2005, 2006; J. L. Racusin et al. 2008; L. Xin et al. 2023); (2) a steeper decay (typically t^{-2}) at very early times, sometimes with a steep rising phase before the steep decay, which is consistent with emission from the GRB reverse shock (P. Meszaros & M. J. Rees 1993, 1999; C. Akerlof et al. 1999; R. Sari & T. Piran 1999; Y.-Z. Fan et al. 2002, 2004; S. Kobayashi & B. Zhang 2003; P. Kumar & A. Panaitescu 2003; B. Zhang et al. 2003; E. Nakar & T. Piran 2004; B. Zhang & S. Kobayashi 2005; Y. C. Zou et al. 2005; R. Harrison & S. Kobayashi 2013; S.-X. Yi et al. 2013, 2020; J. Japelj et al. 2014; H. Gao et al. 2015; S. Zhang et al. 2015; X.-L. Huang et al. 2016; X.-G. Wang et al. 2024); (3) a smooth bump at early times, explained as the onset of afterglow at the blast-wave deceleration radius (E.-W. Liang et al. 2013); (4) a rebrightening feature occasionally observed in some GRBs; and (5) a late-time SN bump. A rapid drop in the X-ray afterglow with a decay index steeper than t^{-3} following the plateau is considered to be evidence of a magnetar collapsing to form a black hole (E. Troja et al. 2007; Y.-Z. Fan et al. 2013; H.-J. Lü et al. 2015; W. Chen et al. 2017; L. Zou et al. 2019). The rebrightening observed in some afterglows can be explained by several theoretical models, including energy injection into the external shock (P. Kumar & T. Piran 2000; B. Zhang & P. Mészáros 2002; J. Granot et al. 2003), a two-component jet (E. Berger et al. 2003; Y. F. Huang et al. 2004; J. L. Racusin et al. 2008), density bumps in the external medium (D. Lazzati et al. 2002; Z. G. Dai & X. F. Wu 2003; E. Nakar & J. Granot 2007), the fallback accretion model (Z. G. Dai & R.-Y. Liu 2012; X.-F. Wu et al. 2013; Y. B. Yu et al. 2015; J. Lin et al. 2020; Z. Yang et al. 2024), and electromagnetic cascade cadiation (X.-G. Wang et al. 2022; R.-J. Xiong et al. 2024).

GRB 151027A is an interesting case that shows two distinct plateaus in the X-ray afterglow and a rebrightening bump in the optical afterglow. Several papers have already been published on GRB 151027A (K. D. Alexander et al. 2016; F. Nappo et al. 2017; D. Primorac et al. 2018; R. Ruffini et al. 2018). F. Nappo et al. (2017) interpreted this afterglow as a standard forward-shock afterglow in the wind medium scenario, adding a late prompt component (G. Ghisellini et al. 2007). In this paper, we present optical observations of GRB 151027A from the 0.76 m Katzman Automatic Imaging Telescope (KAIT) at Lick Observatory (A. V. Filippenko et al. 2001) and the Palomar Observatory 60-inch robotic telescope (P60; S. B. Cenko et al. 2006). Our observations reveal two novel features in GRB 151027A not previously reported: an early onset bump (peaking at $\sim$300 s) and a significant optical rebrightening (peaking at $\sim$2.5 ks). We show that the first X-ray plateau, followed by a sharp drop, can be attributed to a magnetar collapsing to form a black hole, while the second X-ray plateau is likely powered by fallback accretion. To reproduce the optical rebrightening, we resort to the external-shock model with energy injections. The late-time optical bump ($t > 10^6$ s) is well fit by a ^{56}Ni-powered SN light curve. This paper is structured as follows: Section 2 presents our multiwavelength observations; the temporal and spectral analyses are given in Section 3; and Section 4 presents theoretical models of the afterglow light curves. Our conclusions and discussion are presented in Section 5.

2. Observations and Data Reduction

GRB 151027A was triggered by the Swift Burst Alert Telescope (BAT; N. Gehrels et al. 2004; S. D. Barthelmy et al. 2005) on 2015 October 27 at 03:58:24 (denoted as T_0 in this paper; UTC dates are used throughout), with a duration of $T_{90} = 130 \pm 6$ s (A. Maselli et al. 2015; D. M. Palmer et al. 2015). The object was also detected by the Fermi Gamma-ray Burst Monitor (GBM; C. Meegan et al. 2009; K. Toelge et al. 2015) and Konus-Wind (R. L. Aptekar et al. 1995; S. Golenetskii et al. 2015). The Swift X-Ray Telescope (XRT; D. N. Burrows et al. 2005) and the Swift/UVOT (P. W. A. Roming et al. 2005) began observing GRB 151027A at 87 s and 95 s after the BAT trigger, respectively (A. Maselli et al. 2015). We retrieved the Swift/XRT flux light curve from the UK Swift Science Data Centre[14] (P. A. Evans et al. 2010). The UVOT data were processed following the UVOT analysis threads[15] to create the light curve observed by Swift/UVOT.

KAIT responded to GRB 151027A immediately after receiving the burst trigger. Observations were performed using an automatic sequence in the *Clear* (approximately equivalent to *R*; see W. Li et al. 2003), *V*, and *I* filters, with an exposure time of 20 s per frame (W. Zheng & A. V. Filippenko 2015).

P60 automatically responded to the alert for GRB 151027A and began a sequence of imaging in the *i*, *z*, *g*, *r*, and *B* bands (D. A. Perley & S. B. Cenko 2015).

Photometry from KAIT, P60, UVOT, and optical data reported in the Gamma-ray Coordinates Network (GCN) circulars[16] without correction for Galactic extinction is listed in Table 1. The data reported by F. Nappo et al. (2017) and the radio data from the GCN circulars are listed in Table 2. Figure 1 shows the Galactic-extinction-corrected light curve using $E(B - V) = 0.04$ mag derived for the position of GRB 151027A (E. F. Schlafly & D. P. Finkbeiner 2011).

The redshift of GRB 151027A was previously determined to be $z = 0.81$ and presented in the GCN circulars (D. A. Perley et al. 2015) based on a preliminary analysis of an optical spectrum taken with the High Resolution Echelle Spectrometer

[14] https://www.swift.ac.uk/burst_analyser/00661775
[15] https://www.swift.ac.uk/analysis/uvot/index.php
[16] https://gcn.gsfc.nasa.gov/other/151027A.gcn3

Table 1
Photometry of GRB 151027A (Mag)

$T - T_0$[a] (s)	Exp. (s)	Mag[b]	Mag 1σ	Band	Telescope	References
184	20	13.34	0.11	*I*	KAIT	(1)
2684	120	15.05	0.02	*B*	P60	(2)
574	20	14.83	0.05	*B*	Swift/UVOT	(3)
…	…	…	…	…	…	…

Notes.
[a] T–T_0 is the midpoint of each observation. The reference time T_0 is the trigger time of Swift/BAT.
[b] Galactic extinction was not taken into account.
References. (1) This work—KAIT observations; (2) This work—P60 observations; (3) This work—Swift/UVOT observations; (4) D. Xu et al. (2015); (5) Y. Yano et al. (2015); (6) V. P. Hentunen et al. (2015); (7) S. Dichiara et al. (2015); (8) J. Zhang et al. (2015a); (9) E. Sonbas et al. (2015); (10) Z. Cano (2015); (11) A. Moskvitin (2015); (12) D. Sahu & G. Anupama (2015); (13) and A. Pozanenko et al. (2015).

(This table is available in its entirety in machine-readable form in the online article.)

Table 2
Photometry of GRB 151027A (F_ν)

$T - T_0$[a] (s)	Exp. (s)	F_ν[b] (μJy)	$F_\nu 1\sigma$ (μJy)	Band	Telescope	References
24	12	11,080	2053	*R*	RAPTOR	(14), (15)
79	30	9388	1739	*R*	Maidanak AZT-22	(14), (16)
…	…	…	…	…	…	…

Notes.
[a] T–T_0 is the midpoint of each observation. The reference time T_0 is the trigger time of Swift/BAT.
[b] The optical data in this table are taken from F. Nappo et al. (2017), who reported values already corrected for Galactic extinction. The radio data in this table are from F. Nappo et al. (2017) and GCN, which were not corrected for Galactic extinction.
References. (14) F. Nappo et al. (2017); (15) J. Wren et al. (2015); (16) A. Pozanenko et al. (2015); (17) P. Wiggins (2015); (18) L. P. Xin et al. (2015); (19) J. Zhang et al. (2015b); (20) A. Oksanen (2015); (21) Y. Protsyuk & O. Kovalchuk (2015); (22) V. Kozlov et al. (2015); (23) P. Chandra & A. J. Nayana (2015a); (24) P. Chandra & A. J. Nayana (2015b); and (25) T. Laskar et al. (2015).

(This table is available in its entirety in machine-readable form in the online article.)

(HIRES; S. S. Vogt et al. 1994) on the Keck I 10 m telescope in Hawaii.[17] We present here a refined host galaxy systemic redshift of 0.81095 based on a more careful analysis of this spectrum, including air-to-vacuum and heliocentric corrections and more precise line lists. The redshift is estimated via the locations of the centers of the (saturated) Mg II, Mg I, and Ca I lines shown in Figure 2; an uncertainty of ∼0.00015 is inferred from the width of the Mg I and Ca II lines. In the modeling presented in Section 4.5, we adopt the central value of the redshift. The relative uncertainty in the redshift measurement (∼0.02%) is negligible compared with other sources of uncertainty in the modeling; it does not affect the fitting results. We also confirm the presence of numerous Fe II* transitions in the spectrum, clearly demonstrating that the system is the host galaxy and not an intervening absorber. These are blueshifted by about 60 km s^{-1} relative to the estimated centers of the lines used to estimate the systemic redshift, likely due to dynamical motion of the GRB environment within the host galaxy.

[17] The spectrum was obtained on 2015 October 27 at 06:54:53.95 and is publicly available through the W. M. Keck Observatory Archive (PI: Lynne Hillenbrand; Program ID C205Hr; Program title "Characterization of Newly Identified Low-Mass Pre-Main-Sequence Eclipsing Binaries in Orion, NGC 2264, and M35").

3. Temporal and Spectral Analyses

The X-ray afterglow of GRB 151027A consists of a flare and two plateaus, with a steep decay after each plateau. The optical afterglow shows an early smooth bump peaking at ∼300 s, a rebrightening peaking at ∼2.5 ks, and a break at $\sim 4 \times 10^4$ s; all three are observed in the optical light curve but not in the X-ray light curve. To quantify the temporal features of the GRB 151027A afterglow light curves, we fit them with empirical functions, including the single-power-law (SPL), broken-power-law (BPL), and triple-power-law (TPL) functions (E.-W. Liang et al. 2007, 2013; X.-G. Wang et al. 2015). The SPL function is

$$F_1 = F_{01} t^{-\alpha_1}, \tag{1}$$

and the BPL function is

$$F_2 = F_{02}\left[\left(\frac{t}{t_{\rm b,1}}\right)^{\alpha_2\omega_1} + \left(\frac{t}{t_{\rm b,1}}\right)^{\alpha_3\omega_1}\right]^{-1/\omega_1}, \tag{2}$$

where α_1, α_2, and α_3 are the temporal slopes, with negative and positive values representing rising and falling, respectively; $t_{\rm b,1}$ is the break time; and ω_1 describes the sharpness of the break at $t_{\rm b,1}$. The TPL function is

$$F_3 = (F_2^{-\omega_2} + F_4^{-\omega_2})^{-1/\omega_2}, \tag{3}$$

where ω_2 is the sharpness factor of the second break at $t_{\rm b,2}$, and

$$F_4 = F_2(t_{\rm b,2})\left(\frac{t}{t_{\rm b,2}}\right)^{-\alpha_4}. \tag{4}$$

The X-ray flare and the first plateau break sharply, so we adopt $\omega_1 = 10$, while elsewhere we adopt $\omega_1 = \omega_2 = 3$.

The X-ray afterglow was divided into three temporal segments for fitting with BPL functions: the flare (80–200 s); plateau-1, with its subsequent steeper decay (200–500 s); and plateau-2, with its subsequent steeper decay (500–10^6 s). The X-ray flare exhibits slopes of $\alpha_1 = -8.26 \pm 0.48$ (rise phase) and $\alpha_2 = 8.27 \pm 0.22$ (decay phase), with a break at $10^{2.082\pm0.003}$ s. The X-ray plateau-1 exhibits slopes of $\alpha_1 = -0.02 \pm 0.12$ (plateau phase) and $\alpha_2 = 3.41 \pm 0.23$ (steeper decay phase), with a break at $10^{2.533\pm0.008}$ s. The

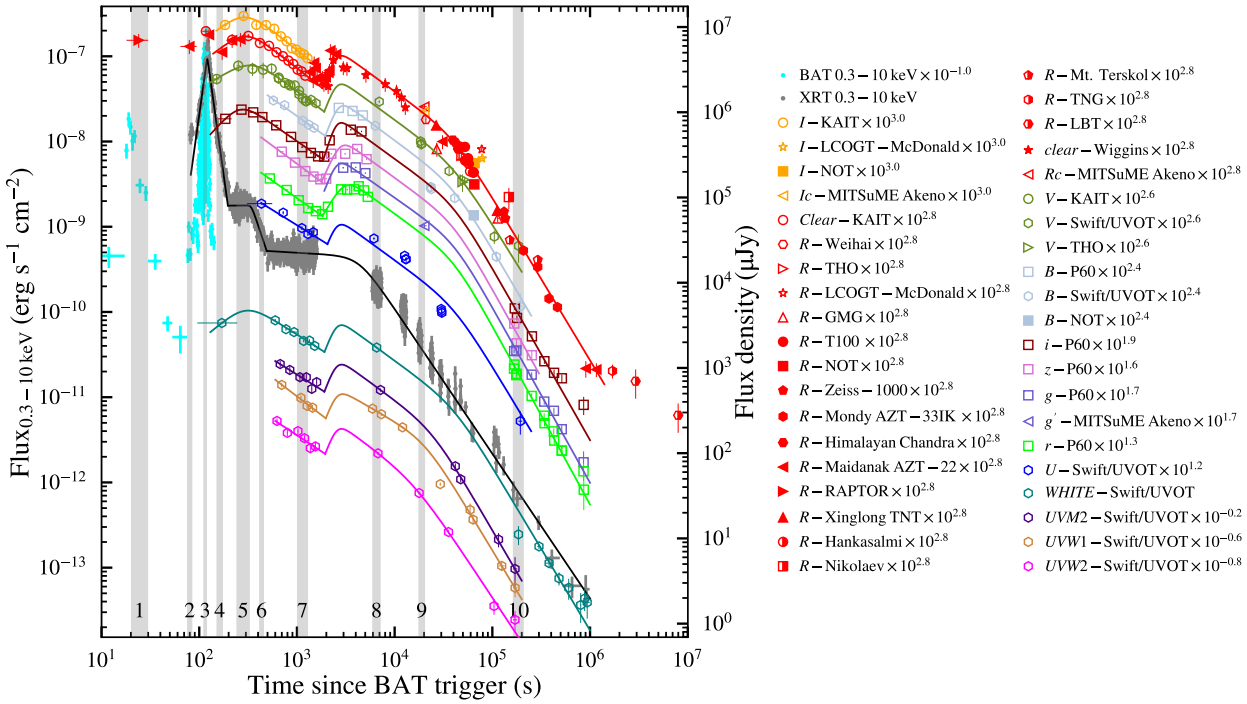

Figure 1. Multiwavelength light curves of GRB 151027A. The gray shaded regions indicate the time intervals used for spectral analysis. The solid curves show best-fit empirical functions to the temporal evolution.

X-ray plateau-2 exhibits slopes of $\alpha_1 = 0.07 \pm 0.03$ (plateau phase) and $\alpha_2 = 1.70 \pm 0.02$ (steeper decay phase), with a break at $10^{3.64\pm0.02}$ s. Although the measured slope $\alpha_1 = 0.07 \pm 0.03$ slightly deviates from 0, it remains within the plateau slope range (0.03–0.3) statistically reported by C.-H. Tang et al. (2019).

The optical afterglow is divided into two temporal segments for fitting, using the beginning of the rebrightening at ∼1.8 ks as the boundary. In data-sparse regions, we fix parameters to the values fitted from the well-sampled *R*-band light curve. For Segment 1, light curves with prepeak data (the *I*, *R*, *V*, *i*, and Swift WHITE bands) are fitted with BPL functions, while light curves with only postpeak data (the *B*, *z*, *r*, *U*, UVM2, UVW1, and UVW2 bands) are fitted with SPL functions. The average slopes before and after the optical peak are $\bar{\alpha}_1 = -0.94 \pm 0.19$ and $\bar{\alpha}_2 = 0.81 \pm 0.07$, respectively, with an average break time of $\bar{t}_{b,1} = 10^{2.47\pm0.04}$ s. These averages are calculated using only unfixed parameters, and the same applies below. For Segment 2, the light curves in each band are fitted using a TPL function. The optical rebrightening bump exhibits average rise and decay slopes of $\bar{\alpha}_3 = -2.81 \pm 0.63$ and $\bar{\alpha}_4 = 0.79 \pm 0.07$, respectively, with an average break time at $\bar{t}_{b,2} = 10^{3.44\pm0.04}$ s. The late-time optical light curve has average decay slopes of $\bar{\alpha}_5 = 1.96 \pm 0.11$ after an average break time at $\bar{t}_{b,3} = 10^{4.38\pm0.16}$ s. Our fitting result is shown in Figure 1, and the fitting parameters for each band are provided in Table 3.

The external-shock model (R. Sari et al. 1998; J. E. Rhoads 1999; R. A. Chevalier & Z.-Y. Li 2000; P. Kumar & T. Piran 2000; J. Granot & R. Sari 2002; B. Zhang & P. Mészáros 2002; H. Gao et al. 2013) predicts that the breaks in afterglow light curves can originate from hydrodynamical evolution, the jet-edge effect, or the passage of spectral break frequencies through the observational band. Breaks from the first two mechanisms are expected to be achromatic, while frequency-related breaks are chromatic. This theoretical framework has been generally supported by comprehensive studies of GRB afterglows (E.-W. Liang et al. 2013; X.-G. Wang et al. 2013, 2015, 2018; L. Li et al. 2015). However, the afterglow of GRB 151027A exhibits complex behavior between the X-ray and optical bands that cannot be explained only by the external-shock model. The X-ray light curve shows an initially bright flare, followed by a plateau and then a steep decay. This is succeeded by another plateau, followed by a steep decay (shallower than the previous one). Previous studies (G. Chincarini et al. 2007, 2010; A. D. Falcone et al. 2007; R. Margutti et al. 2010) indicate that X-ray flares originate from internal emission due to late central engine activity.

X-ray plateaus are typically interpreted with magnetar spin-down models (B. Zhang & P. Mészáros 2001a; N. Bucciantini et al. 2007, 2009; B. D. Metzger et al. 2011; H.-J. Lü & B. Zhang 2014). The X-ray plateau followed by extremely rapid decay is best explained by emission from a magnetar collapsing to form a black hole (E.-W. Liang et al. 2007; E. Troja et al. 2007; A. Rowlinson et al. 2010, 2013). Since we interpret X-ray plateau-1 of GRB 151027A as resulting from a magnetar collapse to form a black hole, X-ray plateau-2 requires an alternative explanation. Energy-injection processes would change the shock dynamics, leading to a shallow decay (plateau) or rebrightening across all wave bands (B. Zhang & P. Mészáros 2002). However, the power-law decline of the optical afterglow remains unchanged during the start of X-ray plateau-2, ruling out energy injection as the origin of X-ray plateau-2. Subsequent spectral fitting indicates distinct origins for the X-ray and optical emission. We propose that fallback accretion (X.-F. Wu et al. 2013) likely powers X-ray plateau-2.

The optical light curve exhibits markedly different behavior. Our subsequent spectral fitting reveals that the optical data prior to 150 s share an origin with the prompt gamma-ray emission.

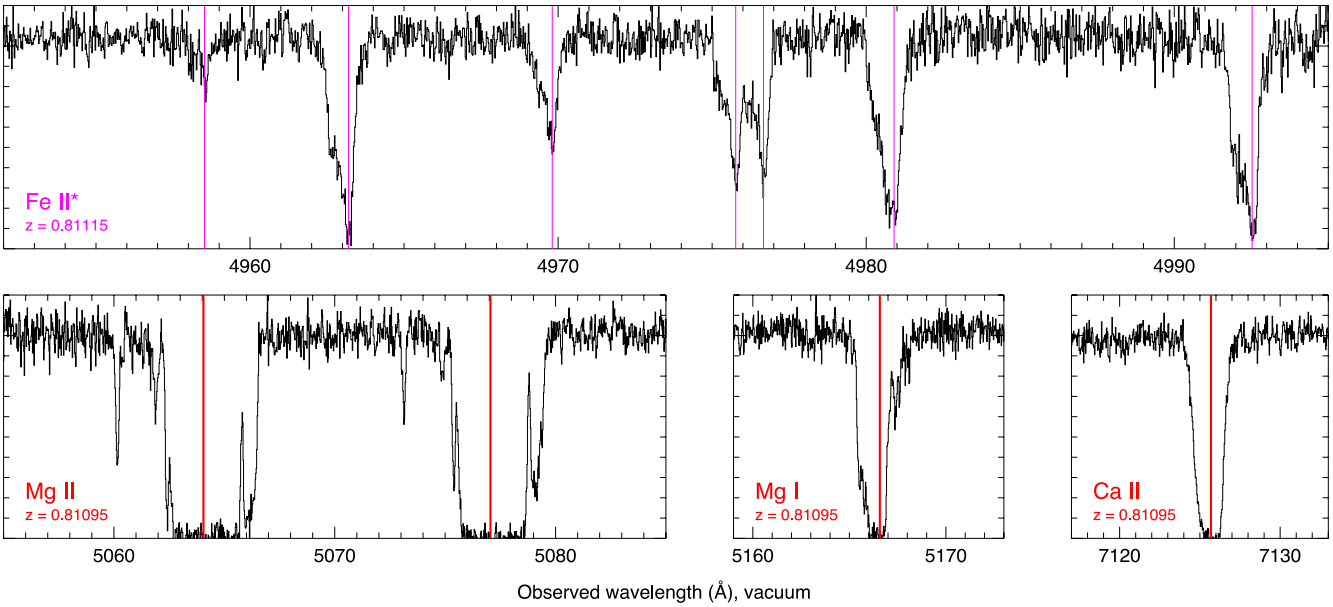

Figure 2. Zoom-ins on regions of the Keck/HIRES spectrum of the afterglow of GRB 151027A, showing strong absorption lines in association with the host system. The top panel reveals fine-structure Fe II* absorption from material near the progenitor site at $z = 0.81115$. The bottom three panels show absorption from transitions of Mg II $\lambda\lambda$2796.35, 2803.53, Mg I λ2852.96, and Ca II λ3934.78, all at $z = 0.81095$, the redshift of GRB 151027A.

Subsequently, a smooth optical bump appears, whose rising phase spans the decay phase of the X-ray flare and X-ray plateau-1, while its declining phase spans both the steep decay following X-ray plateau-1 and the subsequent X-ray plateau-2. The external-shock model predicts an initial onset bump in the afterglow light curve when the blast wave reaches the deceleration radius. Between 2 and 6 ks, when no X-ray data exist, the optical light curve shows significant rebrightening. We use an external-shock model with energy injection to explain the optical rebrightening. After 6 ks, the X-ray flux decays as an SPL, while the optical light curve follows a BPL. Late-time optical observations (after 10^6 s) reveal a bump in the R-band light curve. F. Nappo et al. (2017) proposed that this feature can be interpreted as an SN signature.

We jointly fit the Fermi/GBM (NaI and BGO), the Swift (BAT and XRT), and the optical data with a free normalization constant between NaI, BGO, BAT, and XRT. The spectral fitting package `Xspec` (K. A. Arnaud 1996) was used for the spectral analysis. 10 spectra were extracted, corresponding to the time intervals marked in Figure 1. These spectra were fit using either a power-law model (PL),

$$N(E) = A\left(\frac{E}{1\ \mathrm{keV}}\right)^{-\hat{\Gamma}}, \tag{5}$$

or a power law with exponential cutoff (CPL),

$$N(E) = A\left(\frac{E}{100\ \mathrm{keV}}\right)^{-\hat{\Gamma}} \exp\left(-\frac{E}{E_c}\right), \tag{6}$$

where E is the photon energy, $\hat{\Gamma}$ is the photon index of the power law, A is the normalization, and E_c is the cutoff energy. The peak energy in the $E^2N(E)$ spectrum of the CPL model is given by

$$E_p = (2 - \hat{\Gamma})E_c. \tag{7}$$

Spectra 3 and 4 are located in the X-ray flare. F. Nappo et al. (2017) and R. Ruffini et al. (2018) have clarified that this flare contains a blackbody (BB) spectral component. We model this component in `Xspec` using the bbody model:

$$N(E) = \frac{A \times 8.0525 \times E^2}{(kT)^4[\exp(E/kT) - 1]}, \tag{8}$$

where kT is the BB temperature in keV. All spectral fits account for Galactic and intrinsic photoelectric absorption, as well as dust extinction in the host galaxy. The equivalent hydrogen column density of our Galaxy is $N_H = 3.75 \times 10^{20}$ cm^{-2} in the direction of this burst[18] (R. Willingale et al. 2013). For the host galaxy, we adopt $N_H^{\mathrm{host}} = (4.4^{+0.7}_{-0.6}) \times 10^{21}$ cm^{-2}, derived from the late-time Swift/XRT spectrum.[19] The extinction caused by dust grains in the host galaxy is assumed to be characterized by the extinction curves of the Small Magellanic Cloud (SMC), whose standard value for R_V (the ratio of the total to selective extinction) is $R_{V,\mathrm{SMC}} = 2.93$ (Y. C. Pei 1992). The color excess $E(B - V) = (6.84 \pm 1.42) \times 10^{-2}$ mag of the host galaxy was the fitting result of Spectrum 7, which contains the most optical data. We denote the photon indices derived from gamma-ray (Fermi/GBM and Swift/BAT), X-ray (Swift/XRT), and optical data as $\hat{\Gamma}_\gamma$, $\hat{\Gamma}_X$, and $\hat{\Gamma}_O$, respectively. The spectral fitting results and corresponding parameters are presented in Figure 3 and Table 4.

Spectra 1–3 were jointly fitted with GBM, BAT, XRT, and optical data. We used the CPL model for fitting, because most of the high-energy data points from GBM are upper limits. The optical data are well located in the CPL fitting line, suggesting that the early optical emission (first 150 s) could have the same origin as the high-energy prompt emission and should not be interpreted as the standard external forward-shock afterglow. For Spectra 4–10, the optical data are significantly lower than the PL extrapolation of the XRT fitting results. We therefore fitted the XRT and optical data separately with PL models,

[18] https://www.swift.ac.uk/analysis/nhtot/
[19] https://www.swift.ac.uk/xrt_spectra/00661775/

Table 3
Temporal Parameters of GRB 151027A

Band	α_1	$\log_{10} t_{b,1}$ (s)	α_2	α_3	$\log_{10} t_{b,2}$ (s)	α_4	$\log_{10} t_{b,3}$ (s)	α_5
X-ray flare	-8.26 ± 0.48	2.082 ± 0.003	8.27 ± 0.22	...	...	...	...	...
X-ray plateau-1	-0.02 ± 0.12	2.533 ± 0.008	3.41 ± 0.23	...	...	...	...	...
X-ray plateau-2	0.07 ± 0.03	3.64 ± 0.02	1.70 ± 0.02	...	...	...	...	...
I	-0.87 ± 0.35	2.47 ± 0.06	0.91 ± 0.08	...	...	...	...	...
R	-0.89 ± 0.27	2.48 ± 0.03	0.90 ± 0.05	-3.03 ± 1.85	3.41 ± 0.12	0.83 ± 0.17	4.62 ± 0.13	1.91 ± 0.09
V	-0.71 ± 0.27	2.53 ± 0.06	0.86 ± 0.07	-3.03(fix)	3.41(fix)	0.83(fix)	4.62(fix)	1.85 ± 0.40
B	...	...	0.81 ± 0.05	-3.03(fix)	3.43 ± 0.01	0.84 ± 0.05	4.62(fix)	1.97 ± 0.24
i	-1.28 ± 0.43	2.41 ± 0.04	0.80 ± 0.04	-3.66 ± 0.69	3.41 ± 0.02	0.83 ± 0.15	4.62(fix)	2.02 ± 0.20
z	...	...	0.84 ± 0.05	-2.61 ± 0.35	3.41(fix)	0.83(fix)	4.62(fix)	2.07 ± 0.33
g	...	...	...	-3.03(fix)	3.41(fix)	0.80 ± 0.08	4.62(fix)	2.06 ± 0.12
r	...	...	0.81 ± 0.04	-1.95 ± 0.21	3.49 ± 0.01	0.83(fix)	4.62(fix)	2.10 ± 0.03
U	...	...	0.71 ± 0.07	-3.03(fix)	3.41(fix)	0.83(fix)	4.62(fix)	1.91(fix)
WHITE	-0.96 ± 0.15	2.478(fix)	0.73 ± 0.06	-3.03(fix)	3.41(fix)	0.83(fix)	4.62(fix)	1.92 ± 0.02
UVM2	...	...	0.71 ± 0.12	-3.03(fix)	3.41(fix)	0.83(fix)	4.39 ± 0.04	1.97 ± 0.13
UVW1	...	...	0.87 ± 0.08	-3.03(fix)	3.41(fix)	0.65 ± 0.03	4.31 ± 0.04	1.91 ± 0.07
UVW2	...	...	0.76 ± 0.14	-3.03(fix)	3.41(fix)	0.83(fix)	4.19 ± 0.05	1.74 ± 0.09

Note. "X-ray flare" represents the flare during 80–200 s, with $t_{b,1}$ being its break time; α_1 and α_2 are the rising and falling slopes, respectively. "X-ray plateau-1" represents the first X-ray plateau, with its subsequent steeper decay (200–500 s); α_1 is the slope of the first plateau, α_2 is the slope of its subsequent steeper decay, and $t_{b,1}$ is the end time of the first plateau. "X-ray plateau-2" represents the second plateau, with its subsequent steeper decay (500–10^6 s); α_1 is the slope of the second plateau, α_2 is the slope of its subsequent steeper decay, and $t_{b,1}$ is the end time of the second plateau. For the optical light curve, α_1 and α_2 are respectively the rising and falling slopes of the smooth dump at 150–1800s, and $t_{b,1}$ is its break time; α_3 is the slope of the rebrightening starting at ~1.8 ks, $t_{b,2}$ is the break time of the rebrightening, α_4 and α_5 are respectively the slopes of the following decay and the steeper decay, and $t_{b,3}$ is the break time, likely due to the jet break. For data-sparse bands, parameters were fixed to the values fitted from the well-sampled *R*-band light curve.

revealing distinct origins for the optical and X-ray emission. Figure 4 shows extinction-corrected light curves using the host galaxy $E(B-V) = 0.0684$ mag (E. L. Fitzpatrick 1999).

4. Model and Results

Our multiwavelength analysis establishes that the X-ray and optical afterglow emission of GRB 151027A originate from distinct physical processes. The X-ray plateau is commonly interpreted in the context of magnetar spindown (B. Zhang & P. Mészáros 2001a; H.-J. Lü & B. Zhang 2014; L. Xie et al. 2020). A rapid decline (steeper than t^{-3}) following the plateau is widely considered as evidence of a magnetar collapsing to form a black hole (E. Troja et al. 2007; Y.-Z. Fan et al. 2013; W. Chen et al. 2017; L. Zou et al. 2019). GRB 151027A exhibits two X-ray plateaus, with X-ray plateau-1 followed by a steep decay ($\alpha_2 = 3.41 \pm 0.23$) satisfying this collapse criterion. X. Tian et al. (2025) proposed a supramassive magnetar as the central engine, with a phase transition from a magnetar to a strange star, as well as the cooling and spindown of the strange star, to interpret the observed two-X-ray-plateau emission in GRB 240529A.

In this work, we propose that the first and second plateau emissions in the X-ray afterglow are powered by: (1) magnetar spindown with collapse to form a black hole, before reaching its characteristic spindown timescale; and (2) the fallback accretion of a black hole central engine. The behavior of the optical afterglow differs from that of the X-ray afterglow. The early optical emission (first 150 s) shares the same origin as the high-energy emission, so we will not model it. The subsequent smooth hump observed at ~150–1000 s is consistent with the onset of the external forward-shock model. We resort to the external-shock model with energy injections to reproduce the significant optical rebrightening beginning at ~1.8 ks. Finally, we will model an SN to account for the bump at late times (after 10^6 s), as also suggested by F. Nappo et al. (2017). The following subsections present detailed modeling of these components.

4.1. Magnetar Spindown

The light curve of magnetic dipole radiation from a newly born magnetar typically begins with a plateau. If the magnetar collapses to form a black hole before reaching its characteristic spindown timescale, the magnetic dipole radiation ceases abruptly, resulting in an internal plateau followed by a sharp drop (B. Zhang & P. Mészáros 2001a; E. Troja et al. 2007; H.-J. Lü et al. 2018b). In this scenario, we link the observed isotropic X-ray luminosity to the magnetar spindown through

$$L_{\rm X,iso,sp}(t) = \begin{cases} \frac{\eta_{\rm sp}}{f_{\rm b}} L_{0,\rm sp} & t < t_{\rm col} \\ \frac{\eta_{\rm sp}}{f_{\rm b}} L_{0,\rm sp} \left(\frac{t}{t_{\rm col}}\right)^{-(\hat{\Gamma}_{\rm X}+1)}, & t > t_{\rm col} \end{cases}, \quad (9)$$

where $\eta_{\rm sp}$ is the conversion efficiency from the magnetar's spindown luminosity to X-ray emission (here, we adopt $\eta_{\rm sp} = 0.01$), $f_{\rm b} = 1 - \cos(\theta_{\rm j})$ is the beaming correction factor, $t_{\rm col}$ is the time when the magnetar collapses to form a black hole, and the temporal decay index after $t_{\rm col}$ is $\hat{\Gamma}_X + 1$, due to the curvature effect (P. Kumar & A. Panaitescu 2000; C. D. Dermer 2004). Also, $L_{0,\rm sp}$ represents the characteristic spindown luminosity.

4.2. Fallback Accretion Model

P. Kumar et al. (2008) associated the X-ray plateau with fallback accretion. X.-F. Wu et al. (2013) proposed a fallback accretion model to explain the giant X-ray bump observed in GRB 121027A. Q. Zhang et al. (2018) and L. Zhao et al. (2020) proposed that a second X-ray plateau could be

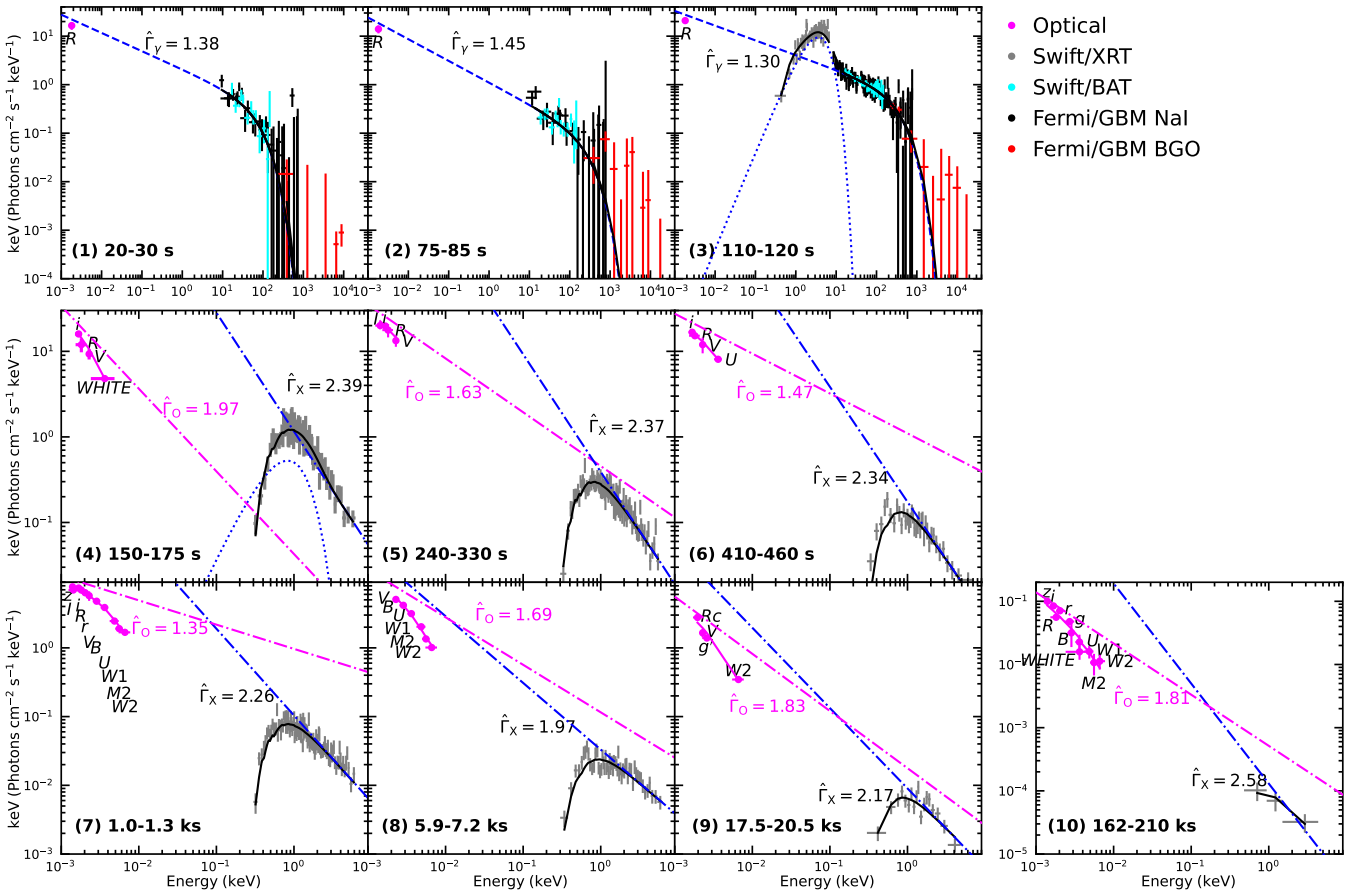

Figure 3. The $EN(E)$ spectra of GRB 151027A. Data are shown for the optical (magenta), Swift/XRT (gray), Swift/BAT (cyan), Fermi/GBM NaI (black), and Fermi/GBM BGO (red). The model components include: CPL (dashed–dashed line), intrinsic PL from X-ray (blue dashed–dotted line), optical (magenta dashed–dotted line), BB (dotted), and composite best fit (solid line).

interpreted by a fallback accretion process. In this work, we apply the fallback accretion model to interpret the second X-ray plateau in GRB 151027A. X.-F. Wu et al. (2013) assumed that during fallback accretion, the Blandford–Znajek (BZ) mechanism powers the relativistic jet by extracting energy from the black hole, significantly enhancing the observed X-ray luminosity. The observed X-ray luminosity can be connected to the BZ power $\dot{E}_{\rm B}$ through

$$\eta_{\rm fb}\dot{E}_{\rm B} = f_{\rm b}L_{\rm X,iso,fb}, \tag{10}$$

where $\eta_{\rm fb}$ represents the efficiency of converting the BZ power into X-ray radiation (here, we adopt $\eta_{\rm fb} = 0.01$). Following X.-F. Wu et al. (2013), we model the fallback accretion rate $\dot{M}$ as a smooth BPL function:

$$\dot{M} = \dot{M}_{\rm p}\left[\frac{1}{2}\left(\frac{t-t_0}{t_{\rm p}-t_0}\right)^{-a_{\rm r}s} + \frac{1}{2}\left(\frac{t-t_0}{t_{\rm p}-t_0}\right)^{-a_{\rm d}s}\right]^{-1/s}, \tag{11}$$

where $\dot{M}_{\rm p}$ is the peak accretion rate, t_0 and $t_{\rm p}$ are respectively the start time and peak time of fallback, s describes the sharpness of the peak, $a_{\rm r} = 1/2$ (A. I. MacFadyen et al. 2001; W. Zhang et al. 2008; Z. G. Dai & R.-Y. Liu 2012), and $a_{\rm d} = -5/3$ (R. A. Chevalier 1989). The dimensionless accretion rate is defined as $\dot{m} = \dot{M}/(M_\odot\ {\rm s}^{-1})$. The BZ jet power from a black hole with black hole dimensionless mass $m_\bullet = M_\bullet/M_\odot$ and angular momentum $J_\bullet$ is given by (H. K. Lee et al. 2000; L.-X. Li 2000; D. X. Wang et al. 2002; J. C. McKinney 2005; W.-H. Lei & B. Zhang 2011; W.-H. Lei et al. 2013):

$$\dot{E}_{\rm B} = 1.7\times10^{50}a_\bullet^2 m_\bullet^2 B_{\bullet,15}F(a_\bullet)\ {\rm erg\ s^{-1}}, \tag{12}$$

where $a_\bullet = J_\bullet c/(GM_\bullet^2)$, with c being the speed of light and G the gravitational constant. The details of the magnetic field strength $B_{\bullet,15}$ threading the black hole horizon and the function $F(a_\bullet)$ are provided by X.-F. Wu et al. (2013).

4.3. External Forward Shock with Energy Injection

It is widely accepted that the onset bump in the afterglow is attributed to blast-wave deceleration, while rebrightening may have multiple origins. Here, we focus our analysis on the energy-injection model (Z. G. Dai & T. Lu 1998; B. Zhang & P. Mészáros 2001a) for the optical rebrightening. We adopt a power-law injection luminosity $L_{\rm inj} = L_{\rm inj,0}t^{-q}$ for $t_{\rm start} < t < t_{\rm end}$, where $L_{\rm inj,0}$ is the normalization luminosity, q is the power-law decay index, and $t_{\rm start}$ and $t_{\rm end}$ respectively denote the injection start time and end time. Since the discovery of GRB afterglows, numerous numerical or semianalytical methods have been proposed to model them (P. Mészáros & M. J. Rees 1997; A. Panaitescu et al. 1998; R. Sari et al. 1998; Y. F. Huang et al. 1999, 2000; C. D. Dermer et al. 2000; B. Zhang & P. Mészáros 2001b; J. Granot & R. Sari 2002; J. Granot & P. Kumar 2003; H. van Eerten et al. 2012; W.-H. Lei et al. 2016; J. Granot et al. 2018; G. Ryan et al. 2020; J. Ren et al. 2024; H. Wang et al. 2024;

Table 4
Spectral Fitting Results for GRB 151027A

#	Data[a]	Time Interval (ks)	Model	$\hat{\Gamma}_\gamma$[b]	$\hat{\Gamma}_X$[b]	$\hat{\Gamma}_O$[b]	E_p (keV)	kT (keV)
1	B+G+O	0.020–0.030	CPL	1.38 ± 0.03	⋯	⋯	47 ± 11	⋯
2	B+G+O	0.075–0.085	CPL	1.45 ± 0.03	⋯	⋯	154 ± 116	⋯
3	B+G+X+O	0.110–0.120	CPL+BB	1.30 ± 0.01	⋯	⋯	244 ± 29	1.29 ± 0.08
4	X+O	0.150–0.175	PL+BB	⋯	2.39 ± 0.07	1.97 ± 0.04	⋯	0.29 ± 0.03
5	X+O	0.240–0.330	PL	⋯	2.37 ± 0.03	1.63 ± 0.34	⋯	⋯
6	X+O	0.410–0.460	PL	⋯	2.34 ± 0.07	1.47 ± 0.04	⋯	⋯
7	X+O	1.0–1.3	PL	⋯	2.26 ± 0.04	1.35 ± 0.11	⋯	⋯
8	X+O	5.9–7.2	PL	⋯	1.97 ± 0.05	1.69 ± 0.04	⋯	⋯
9	X+O	17.5–20.5	PL	⋯	2.17 ± 0.10	1.83 ± 0.05	⋯	⋯
10	X+O	162–210	PL	⋯	2.58 ± 0.47	1.81 ± 0.11	⋯	⋯

Notes.
[a] Spectral data used in the fit: B = Swift/BAT, G = Fermi/GBM, X = Swift/XRT, and O = optical.
[b] $\hat{\Gamma}_\gamma$, $\hat{\Gamma}_X$, and $\hat{\Gamma}_O$ represent the photon indices inferred from gamma-ray data (GBM and BAT), X-ray data (XRT), and optical data, respectively.

Y. Kusafuka et al. 2025; V. Nedora et al. 2025). Here, we adopt `VegasAfterglow` (v1.0.0; Y. Wang et al. 2026) to compute the radiation from the external forward shock in GRB 151027A. `VegasAfterglow` self-consistently solves forward- and reverse-shock dynamics and calculates synchrotron radiation, including synchrotron self-absorption. We consider a top-hat jet structure that propagates into an interstellar medium environment. For calculating the forward-shock radiation, we treat the energy-injection parameters ($L_{\rm inj,0}$, q, $t_{\rm start}$, and $t_{\rm end}$) and the following parameters as free: the isotropic-equivalent energy ($E_{\rm iso}$),[20] the initial Lorentz factor of the jet (Γ_0), the fractions of the shock energy that go to electrons (ϵ_e) and magnetic fields (ϵ_B) in the forward shock, the opening half-angle of the jet (θ_j), the electron spectral index (p), and the number density of the ambient medium (n_0). The viewing angle and the fraction of accelerated electrons are fixed at $\theta_v = 0$ and $\xi_e = 1$, respectively. Details of `VegasAfterglow` are taken from Y. Wang et al. (2026).

4.4. SN

We model the SN light curve using the ^{56}Ni cascade decay model (W. D. Arnett 1982). The spectral energy distribution of the SN is assumed to follow a BB. The flux density at frequency ν, as observed at a luminosity distance D_L, is given by

$$f_\nu = \frac{2\pi h\nu^3}{c^2}\frac{1}{e^{h\nu/kT_{\rm phot}}-1}\frac{R_{\rm phot}^2}{D_L^2}\ {\rm erg\ s^{-1}\ cm^{-2}\ Hz^{-1}}, \quad (13)$$

where h is Planck's constant, k is Boltzmann's constant, and $T_{\rm phot}$ and $R_{\rm phot}$ are respectively the temperature (in Kelvins) and the radius of the photosphere. The temperature $T_{\rm phot}$ and radius $R_{\rm phot}$ are given by (M. Nicholl et al. 2017):

$$T_{\rm phot}(t) = \begin{cases} \left(\frac{L_{\rm SN}(t)}{4\pi\sigma v_{\rm phot}^2 t^2}\right)^{\frac{1}{4}}, & \left(\frac{L_{\rm SN}(t)}{4\pi\sigma v_{\rm phot}^2 t^2}\right)^{\frac{1}{4}} > T_{\rm f} \\ T_{\rm f}, & \left(\frac{L_{\rm SN}(t)}{4\pi\sigma v_{\rm phot}^2 t^2}\right)^{\frac{1}{4}} \leqslant T_{\rm f} \end{cases}, \quad (14)$$

$$R_{\rm phot}(t) = \begin{cases} v_{\rm phot}\, t, & \left(\frac{L_{\rm SN}(t)}{4\pi\sigma v_{\rm phot}^2 t^2}\right)^{\frac{1}{4}} > T_{\rm f} \\ \left(\frac{L_{\rm SN}(t)}{4\pi\sigma T_{\rm f}^4}\right)^{\frac{1}{2}}, & \left(\frac{L(t)}{4\pi\sigma v_{\rm phot}^2 t^2}\right)^{\frac{1}{4}} \leqslant T_{\rm f} \end{cases}, \quad (15)$$

where σ is the Stefan–Boltzmann constant, $T_{\rm f}$ is the final plateau temperature, and $v_{\rm phot}$ is the photospheric velocity. We assume that $v_{\rm phot} \approx v_{\rm ej,SN}$, where $v_{\rm ej,SN}$ is the velocity of the SN ejecta. The SN luminosity $L_{\rm SN}$ can be written as (W. D. Arnett 1982; S. Q. Wang et al. 2015a; D.-F. Kong et al. 2024)

$$L_{\rm SN}(t) = e^{-(t/t_{\rm diff})^2}\int_0^t 2P_{\rm Ni}(t')\frac{t'}{t_{\rm diff}}e^{(t'/t_{\rm diff})^2}(1-e^{-At^{-2}})\frac{{\rm d}t'}{t_{\rm diff}}, \quad (16)$$

where

$$t_{\rm diff} = \left(\frac{2\kappa M_{\rm ej,SN}}{\beta_{\rm SN} c v_{\rm ej,SN}}\right)^{1/2} \quad (17)$$

is the diffusion time, and

$$A = \frac{3\kappa_\gamma M_{\rm ej,SN}}{4\pi v_{\rm ej,SN}^2} \quad (18)$$

is the leakage parameter (S. Q. Wang et al. 2015a). The parameter $\beta_{\rm SN}$ has a typical value of 13.8 (W. D. Arnett 1982); $M_{\rm ej,SN}$, $v_{\rm ej,SN}$, κ, and κ_γ represent the SN ejecta mass, the expansion velocity of the SN ejecta, the optical opacity to optical photons, and the opacity to gamma rays, respectively. We fix the value of κ to be 0.07 cm^2 g^{-1} in this work. The total power $P_{\rm Ni}$ from the radioactivity of ^{56}Ni and its daughter nucleus ^{56}Co can be written as (S. Q. Wang et al. 2015b):

$$P_{\rm Ni}(t) = \epsilon_{\rm Ni} M_{\rm Ni} e^{-t/t_{\rm Ni}} + \epsilon_{\rm Co} M_{\rm Ni}\frac{e^{-t/t_{\rm Co}} - e^{-t/t_{\rm Ni}}}{1 - t_{\rm Ni}/t_{\rm Co}}\ {\rm erg\ s^{-1}}, \quad (19)$$

where $M_{\rm Ni}$ is the amount of ^{56}Ni formed in the explosion, $\epsilon_{\rm Ni} = 3.9 \times 10^{10}$ erg g^{-1} s^{-1}, $t_{\rm Ni} = 8.8$ days, $\epsilon_{\rm Co} = 6.8 \times 10^9$ erg g^{-1} s^{-1}, and $t_{\rm Co} = 111.3$ days.

[20] One needs to note that `VegasAfterglow` adopted $E_{\rm iso}$ (which includes the rest-mass energy), rather than the isotropic kinetic energy ($E_{\rm K,iso}$), to simulate the afterglow.

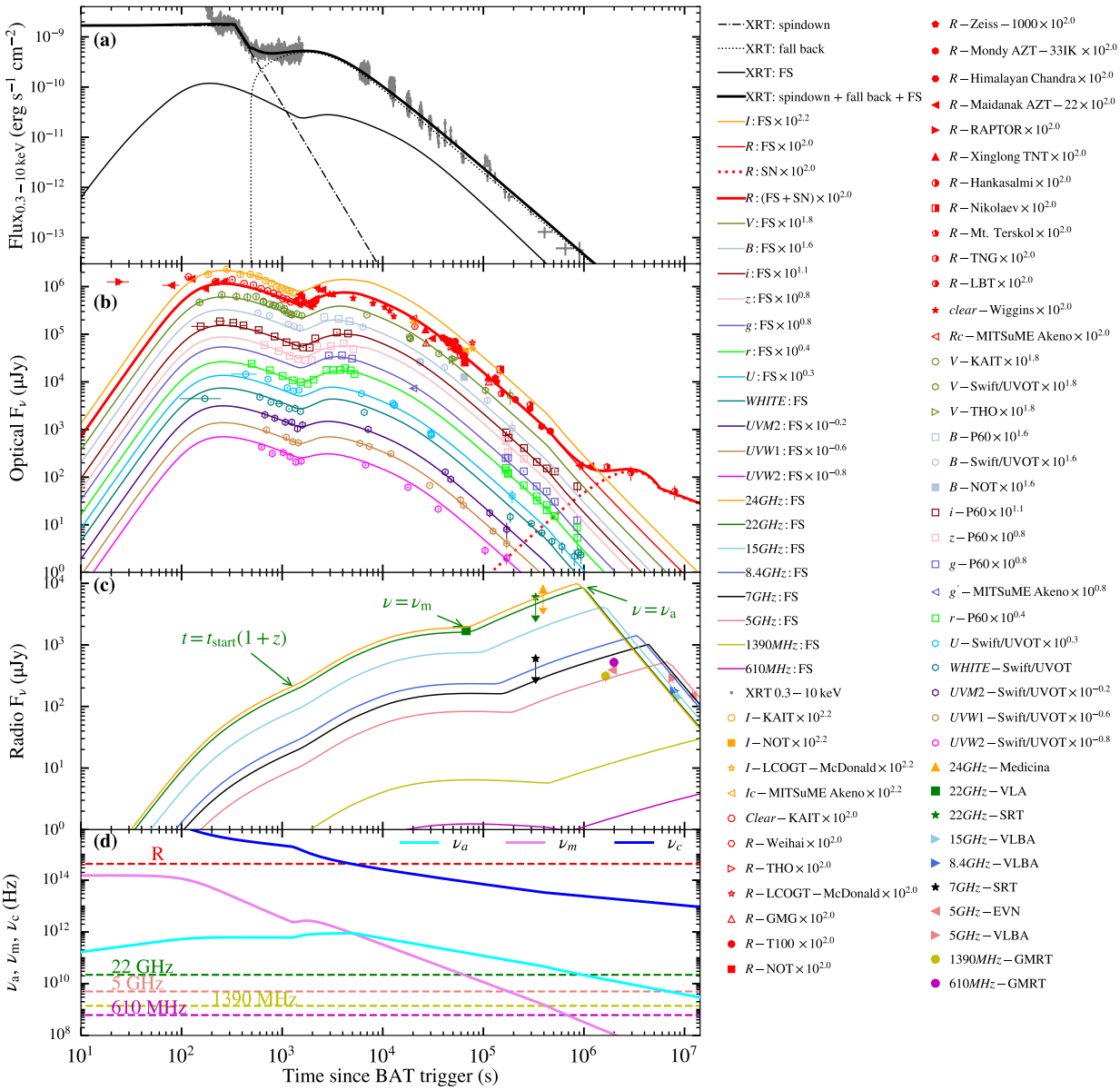

Figure 4. Best-fitting results of the energy-injection model for the afterglow light curves of GRB 151027A. (a) X-ray afterglow. Swift/XRT data (gray points). Model components: magnetar spindown (dashed–dotted line), fallback accretion (dotted line), external shock (thin solid line), and total best fit (thick solid line). (b) Optical afterglow. External-shock component (thin solid line), SN (dotted line), and total best fit (thick solid line). (c) Radio afterglow. External-shock component (thin solid line). (d) Evolution of characteristic frequencies in the observer frame: ν_a, ν_m, and ν_c (solid lines), along with several observed frequencies (dashed lines) —R band (optical), 22 GHz, 5 GHz, 1390 MHz, and 610 MHz (radio).

4.5. Fitting and Results

We performed Markov Chain Monte Carlo (MCMC) sampling using the `emcee` package (D. Foreman-Mackey et al. 2013) to explore the parameter space, with 52 walkers, running for 10,000 steps, and discarding the initial 1000 steps as burn-in. In the MCMC sampling process, the log-likelihood was given by (D. W. Hogg et al. 2010)

$$\ln \mathcal{L} = -\frac{1}{2}\sum_i \sum_j \left[\left(\frac{F_{i,j}^{\rm obs} - F_{i,j}^{\rm mod}}{\sigma_{{\rm tot},i,j}} \right)^2 + \ln\left(2\pi\sigma_{{\rm tot},i,j}^2\right) \right] \quad (20)$$

and

$$\sigma_{{\rm tot},i,j}^2 = \sigma_{i,j}^2 + \left(f F_{i,j}^{\rm mod}\right)^2, \quad (21)$$

where $F_{i,j}^{\rm obs}$ and $\sigma_{i,j}$ represent the observed data and its measurement uncertainty, respectively, for the jth data point in the ith band, and $F_{i,j}^{\rm mod}$ is the value predicted by our model. We model potential multiplicative noise or intrinsic scatter proportional to the flux level by introducing a dimensionless scale parameter f: $f = f_{\rm x}$ for X-ray data, while $f = f_{\rm o}$ for optical and radio data.

Figures 4(a), (b), and (c) show the best-fit light curves overlaid on observational data, with the posterior distributions of parameters presented in Figure 5. Table 5 reports the values of the best-fit parameters, including their corresponding priors and bounds, as well as the posterior median values with 1σ errors for each parameter. We also list the best-fit parameters here: for the external-shock model, $\log_{10}E_{\rm iso} = 54.24^{+0.17}_{-0.15}$ erg, $\log_{10}\Gamma_0 = 2.15^{+0.02}_{-0.03}$, $\log_{10}\epsilon_{\rm e} = -2.48^{+0.11}_{-0.12}$, $\log_{10}\epsilon_{\rm B} = -2.62^{+0.11}_{-0.11}$,

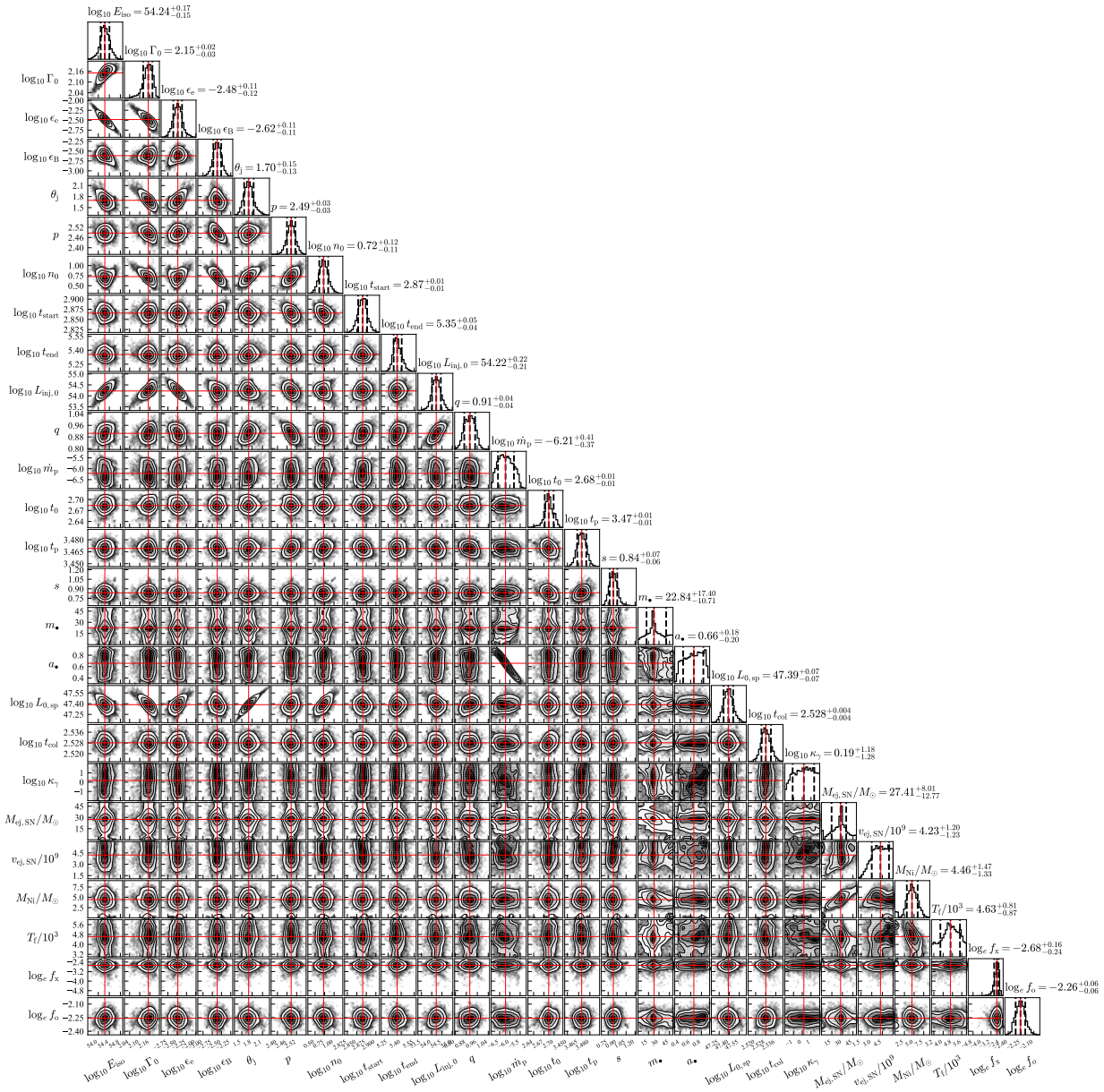

Figure 5. Corner plot of posterior distributions for the energy-injection model parameters. The corresponding light curves are shown in Figure 4.

$\theta_{\rm j} = 1.70^{+0.15\circ}_{-0.13}$, $p = 2.49^{+0.03}_{-0.03}$, $\log_{10} n_0 = 0.72^{+0.12}_{-0.11}$ cm^{-3}, $\log_{10} t_{\rm start} = 2.87^{+0.01}_{-0.01}$ s, $\log_{10} t_{\rm end} = 5.35^{+0.05}_{-0.04}$ s, $\log_{10} L_{\rm inj,0} = 54.22^{+0.22}_{-0.21}$ erg s^{-1}, and $q = 0.91^{+0.04}_{-0.04}$; for the fallback accretion model, $\log_{10} \dot{m}_{\rm p} = -6.21^{+0.41}_{-0.37}$, $\log_{10} t_0 = 2.68^{+0.01}_{-0.01}$ s, $\log_{10} t_{\rm p} = 3.47^{+0.01}_{-0.01}$ s, $s = 0.84^{+0.07}_{-0.06}$, $m_\bullet = 22.84^{+17.40}_{-10.71}$, and $a_\bullet = 0.66^{+0.18}_{-0.20}$; for the magnetar spindown model, $\log_{10} L_{0,\rm sp} = 47.39^{+0.07}_{-0.07}$ erg s^{-1}, $\log_{10} t_{\rm col} = 2.528^{+0.004}_{-0.004}$ s; and for the SN, $\log_{10} \kappa_\gamma = 0.19^{+1.18}_{-1.28}$ cm^2 g^{-1}, $M_{\rm ej,SN} = 27.41^{+8.01}_{-12.77} M_\odot$, $v_{\rm ej,SN} = (4.23^{+1.20}_{-1.23}) \times 10^9$ cm s^{-1}, and $M_{\rm Ni} = 4.46^{+1.47}_{-1.33} M_\odot$, $T_{\rm f} = (4.63^{+0.81}_{-0.87}) \times 10^3$ K. According to Figure 4, one can find that we successfully reproduce the multiwavelength afterglow light curves of GRB 151027A.

The Giant Metrewave Radio Telescope (GMRT) observations at 1390 MHz (P. Chandra & A. J. Nayana 2015a) and 610 MHz (P. Chandra & A. J. Nayana 2015b) show significant deviations from the model predictions. As noted by F. Nappo et al. (2017), these GMRT detections may be contaminated by a nearby bright unresolved source (private communication between P. Chandra and F. Nappo). Alternatively, the excess emission in the GMRT bands could also be explained by emission from a wider, slower outflow component, such as a "cocoon" (D. Lazzati et al. 2018; H. Hamidani et al. 2025; J.-H. Zheng et al. 2025). However, with only two data points in the GMRT bands, current observations lack the spectral and temporal coverage necessary to robustly discriminate between this interpretation, the background contamination hypothesis proposed by F. Nappo et al. (2017), and other possibilities.

In Figure 4(d), we show the evolution of the characteristic frequencies of the synchrotron emission in the external shock—the self-absorption $\nu_{\rm a}$ (cyan solid line), the characteristic synchrotron frequency $\nu_{\rm m}$ for the minimum energy of the injected electrons (violet solid line), and the cooling frequency $\nu_{\rm c}$ (blue solid line). At early times, the frequency ordering is $\nu_{\rm a} < \nu_{\rm m} < \nu_{\rm c}$. At $\sim 5.0 \times 10^3$ s, $\nu_{\rm m}$ crosses $\nu_{\rm a}$ (i.e., $\nu_{\rm m} = \nu_{\rm a}$), after which the ordering becomes $\nu_{\rm m} < \nu_{\rm a} < \nu_{\rm c}$ for the

Table 5
Parameter Estimation Priors and Marginalized Posteriors for GRB 151027A Afterglow Model

Parameter	Unit	Physical Mechanism	Bounds	Posterior
$\log_{10}E_{\rm iso}$	erg	External shock	[50, 56]	$54.24^{+0.17}_{-0.15}$
$\log_{10}\Gamma_0$	⋯	External shock	[1.3, 3]	$2.15^{+0.02}_{-0.03}$
$\log_{10}\epsilon_{\rm e}$	⋯	External shock	[−6, −0.2]	$-2.48^{+0.11}_{-0.12}$
$\log_{10}\epsilon_{\rm B}$	⋯	External shock	[−6, −0.2]	$-2.62^{+0.11}_{-0.11}$
$\theta_{\rm j}$	deg	External shock	[0.3, 10]	$1.70^{+0.15}_{-0.13}$
p	⋯	External shock	[2, 3]	$2.49^{+0.03}_{-0.03}$
$\log_{10}n_0$	$\rm cm^{-3}$	External shock	[−2, 3]	$0.72^{+0.12}_{-0.11}$
$\log_{10}t_{\rm start}$	s	External shock	[2.5, 3.5]	$2.87^{+0.01}_{-0.01}$
$\log_{10}t_{\rm end}$	s	External shock	[$\log_{10}t_{\rm start}$, 8]	$5.35^{+0.05}_{-0.04}$
$\log_{10}L_{\rm inj,0}$	$\rm erg\ s^{-1}$	External shock	[45, 59]	$54.22^{+0.22}_{-0.21}$
q	⋯	External shock	[−3, 3]	$0.91^{+0.04}_{-0.04}$
$\log_{10}\dot{m}_{\rm p}$	⋯	Fallback accretion	[−12, −2]	$-6.21^{+0.41}_{-0.37}$
$\log_{10}t_0$	s	Fallback accretion	[$\log_{10}t_{\rm col}$, $\log_{10}t_{\rm p}$]	$2.68^{+0.01}_{-0.01}$
$\log_{10}t_{\rm p}$	s	Fallback accretion	[2.5, 4]	$3.47^{+0.01}_{-0.01}$
s	⋯	Fallback accretion	[0, 3]	$0.84^{+0.07}_{-0.06}$
$m_\bullet$	⋯	Fallback accretion	[0, 50]	$22.84^{+17.40}_{-10.71}$
$a_\bullet$	⋯	Fallback accretion	[0, 1]	$0.66^{+0.18}_{-0.20}$
$\log_{10}L_{0,\rm sp}$	$\rm erg\ s^{-1}$	Magnetar spindown	[40, 55]	$47.39^{+0.07}_{-0.07}$
$\log_{10}t_{\rm col}$	s	Magnetar spindown	[2.3, 2.7]	$2.528^{+0.004}_{-0.004}$
$\log_{10}\kappa_\gamma$	$\rm cm^2\ g^{-1}$	SN	[−2, 2]	$0.19^{+1.18}_{-1.28}$
$M_{\rm ej,SN}$	$M_\odot$	SN	[0.2, 50]	$27.41^{+8.01}_{-12.77}$
$v_{\rm ej,SN}$	$10^9\ \rm cm\ s^{-1}$	SN	[1, 6]	$4.23^{+1.20}_{-1.23}$
$M_{\rm Ni}$	$M_\odot$	SN	[$0.01M_{\rm ej,SN}$, $0.5M_{\rm ej,SN}$]	$4.46^{+1.47}_{-1.33}$
$T_{\rm f}$	10^3 K	SN	[3, 6]	$4.63^{+0.81}_{-0.87}$
$\log_e f_{\rm x}$	⋯	⋯	[−10, 10]	$-2.68^{+0.16}_{-0.24}$
$\log_e f_{\rm o}$	⋯	⋯	[−10, 10]	$-2.26^{+0.06}_{-0.06}$

remainder of the evolution. Specifically, $\nu_{\rm c}$ crosses the R band at 4.7×10^3 s, $\nu_{\rm m}$ crosses 22 GHz at 6.4×10^4 s, and $\nu_{\rm a}$ subsequently crosses 22 GHz at $\sim9.7\times10^5$ s. After $\nu_{\rm m}$ crosses through the radio band, the radio light curves rise with a steeper slope, peaking when the observed frequency equals $\nu_{\rm a}$ between $\sim10^6$ s and 10^7 s (Figure 4(c)). This is different from the radio bump around 10^4 s, which is produced by the energy injection. The radio bump begins at $t = t_{\rm start}(1+z)\approx1.3\times10^3$ s when the energy injection starts, and ends at the time when the observed frequency equals $\nu_{\rm m}$.

It should be noted that the corner plots from the MCMC analysis (Figure 5) demonstrate several two-parameter degeneracies. Here are several examples:

1. *The* $\log_{10}E_{\rm iso}-\log_{10}\epsilon_{\rm e}$ *degeneracy.* The afterglow luminosity is positively correlated with both $E_{\rm iso}$ and $\epsilon_{\rm e}$. For a given observed luminosity, a higher $E_{\rm iso}$ requires a lower $\epsilon_{\rm e}$ to reproduce the measured flux, resulting in the negative degeneracy visible in Figure 5.
2. *The* $\log_{10}E_{\rm iso}-\log_{10}L_{\rm inj,0}$ *degeneracy.* A jet with a higher initial isotropic-equivalent energy requires a correspondingly higher injection luminosity to noticeably alter its dynamics and thus produce an observable rebrightening in the afterglow light curve.
3. *The* $\theta_{\rm j}-\log_{10}L_{0,\rm sp}$ *degeneracy.* For the magnetar component, the observed isotropic luminosity ($L_{\rm X,iso,sp}$) is inversely proportional to the jet solid angle and directly proportional to the characteristic spindown luminosity ($L_{0,\rm sp}$): $L_{\rm X,iso,sp}\propto L_{0,\rm sp}/(1-\cos\theta_{\rm j})\propto L_{0,\rm sp}/\theta_{\rm j}^2$. Consequently, a fixed $L_{\rm X,iso,sp}$ leads to a strong negative correlation between $\theta_{\rm j}$ and $L_{0,\rm sp}$.
4. *The* $\log_{10}\dot{m}_{\rm p}-a_\bullet$ *degeneracy.* Within the fallback accretion model, both a higher fallback accretion rate and a higher black hole spin can increase the BZ jet power. This creates a strong negative correlation between $\log_{10}\dot{m}_{\rm p}$ and $a_\bullet$.

However, the corner plots show that $\epsilon_{\rm e}$ and $\epsilon_{\rm B}$ are not strongly degenerate. This is because the three characteristic frequencies ($\nu_{\rm a}$, $\nu_{\rm m}$, and $\nu_{\rm c}$) cross different observational bands at different times (see Figure 4(d)). These characteristic frequencies have different functional dependencies on $\epsilon_{\rm e}$ and $\epsilon_{\rm B}$ (R. Sari et al. 1998; J. Granot & R. Sari 2002), providing combined constraints that help to break the degeneracy.

Higher-order degeneracies involving more than two parameters may also exist, although such complex correlations are not captured by the corner plots. In addition, the SN contribution is constrained by only a limited number of late-time R-band data points. Consequently, the SN-related parameters exhibit broad posterior distributions, reflecting significant degeneracy. The fit presented here therefore represents one viable parameter set rather than a unique solution. Under these circumstances, other parameter combinations within the same model could likely reproduce the observations, and alternative models, such as a two-component jet for the optical rebrightening, may also account for the data.

5. Discussion and Conclusions

This study presents multiwavelength observations and analysis of GRB 151027A, revealing its complex temporal evolution. We detected a distinct optical onset bump (peaking

at ∼300 s), followed by optical rebrightening (peaking at ∼2.5 ks). GRB 151027A was observed across multiple wavelengths, from radio up to gamma-ray emission. It exhibits a majority of the characteristic features observed in GRBs, including prompt gamma-ray emission, prompt optical emission, an initial optical afterglow onset bump, optical rebrightening, a late-time SN bump, as well as an X-ray flare and two X-ray plateaus. Both spectral analysis and theoretical modeling suggest that the X-ray and optical emission originate from distinct physical mechanisms. An additional emission component is required to explain the X-ray afterglow.

Our interpretation framework suggests that the magnetar spindown model can account for the first X-ray plateau, while fallback accretion can power the second X-ray plateau. Time-resolved spectral analysis indicates that the early optical emission (first 150 s) shares spectral properties with the high-energy gamma-ray emission, suggesting a common origin in internal dissipation processes. The energy-injection model successfully reproduces the optical rebrightening. The late-time optical bump ($>10^6$ s) is well modeled by an SN powered by ^{56}Ni decay.

GRB 151027A presents a complete evolutionary sequence for an LGRB. Here, we infer its lifetime as follows. A massive star (maybe a Wolf–Rayet star) collapses to form a rapidly rotating magnetar, which drives a relativistic jet. Internal dissipation within the jet produces the prompt gamma-ray and optical emission, through mechanisms such as internal shocks or magnetic reconnection. The jet interacts with the circumburst medium, generating a relativistic forward shock. Concurrently, central engine activity produces an X-ray flare. Spindown luminosity from the magnetar creates the first X-ray plateau. The subsequent collapse of the magnetar to form a black hole triggers a steep decay in the X-ray light curve. As the jet decelerates, it produces the smooth optical onset bump. Subsequently, energy injection into the forward shock causes the optical rebrightening. The fallback accretion onto the black hole results in the second X-ray plateau. The energy injection may originate from either the later ejecta (which produced the X-ray flare through internal dissipation) catching up with the preceding and decelerating ejecta or from Poynting flux powered by late-time fallback accretion onto the central black hole. Finally, as the afterglow fades, thermal emission from the associated SN emerges as a late-time bump. This study demonstrates how multiwavelength analysis can clarify complex central engine behavior, revealing connections between prompt emission, afterglow features, and progenitor properties.

Acknowledgments

This work is supported by the Guangxi Natural Science Foundation (2026GXNSFFA00640004), the Guangxi Science and Technology Innovation Platform Program (Leitai Action Plan, Grant No. Guike LT2600640026), Guangxi Key R&D Program (Guangxi Funeng Action Plan, Grant No. FN2504240030), the "Guangxi Highland of Innovation Talents" Program, the National Natural Science Foundation of China (grants 12494573, 12373042, U1938201, 12494574, 12494575, 12273005 and 12133003), the Bagui Scholars Programme (X.-G.W., grant GXR-6BG2424001), and the special funding for Guangxi Bagui Youth Scholars (Da-Bin Lin). The research group of A.V.F. at U.C. Berkeley received financial assistance from the Christopher R. Redlich Fund, as well as donations from Gary and Cynthia Bengier, Clark and Sharon Winslow, Alan Eustace and Kathy Kwan (W.Z. is a Bengier–Winslow–Eustace Specialist in Astronomy), and many other donors.

This work has made use of data supplied by the UK Swift Science Data Centre at the University of Leicester. KAIT and its ongoing operation were made possible by donations from Sun Microsystems, Inc., the Hewlett-Packard Company, AutoScope Corporation, the Lick Observatory, the U.S. National Science Foundation, the University of California, the Sylvia & Jim Katzman Foundation, and the TABASGO Foundation. Research at the Lick Observatory is partially supported by a generous gift from Google. Some of the data presented herein were obtained at the W. M. Keck Observatory, which is operated as a scientific partnership among the California Institute of Technology, the University of California, and NASA; the observatory was made possible by the generous financial support of the W. M. Keck Foundation. This research has made use of the Keck Observatory Archive (KOA), which is operated by the W. M. Keck Observatory and the NASA Exoplanet Science Institute (NExScI), under contract with NASA. We thank Lynne Hillenbrand for obtaining the Keck/HIRES observations and for providing us with the reduced spectrum presented here.

ORCID iDs

Liang-Jun Chen https://orcid.org/0009-0007-7188-3196
Xiang-Gao Wang https://orcid.org/0000-0001-8411-8011
Hou-Jun Lü https://orcid.org/0000-0001-6396-9386
WeiKang Zheng https://orcid.org/0000-0002-2636-6508
Daniel A. Perley https://orcid.org/0000-0001-8472-1996
Da-Bin Lin https://orcid.org/0000-0003-1474-293X
Yihan Wang https://orcid.org/0000-0002-8614-8721
De-Feng Kong https://orcid.org/0009-0000-6816-654X
You-Dong Hu https://orcid.org/0000-0002-7400-4608
S. Bradley Cenko https://orcid.org/0000-0003-1673-970X
Hong-Bang Liu https://orcid.org/0000-0003-1695-3263
Fei Xie https://orcid.org/0000-0002-0105-5826
En-Wei Liang https://orcid.org/0000-0002-7044-733X
Bing Zhang https://orcid.org/0000-0002-9725-2524
Alexei V. Filippenko https://orcid.org/0000-0003-3460-0103

References

Abbott, B. P., Abbott, R., Abbott, T. D., et al. 2017, ApJL, 848, L12
Abdalla, H., Adam, R., Aharonian, F., et al. 2019, Natur, 575, 464
Abe, H., Abe, S., Acciari, V. A., et al. 2024, MNRAS, 527, 5856
Akerlof, C., Balsano, R., Barthelmy, S., et al. 1999, Natur, 398, 400
Alexander, K. D., Laskar, T., Fong, W., Berger, E., & Zauderer, B. A. 2016, in Eighth Huntsville Gamma-Ray Burst Symposium (Huntsville, AL) 4022
Aptekar, R. L., Frederiks, D. D., Golenetskii, S. V., et al. 1995, SSRv, 71, 265
Arnaud, K. A. 1996, ASPC, 101, 17
Arnett, W. D. 1982, ApJ, 253, 785
Barthelmy, S. D., Barbier, L. M., Cummings, J. R., et al. 2005, SSRv, 120, 143
Berger, E., Kulkarni, S. R., Pooley, G., et al. 2003, Natur, 426, 154
Bucciantini, N., Quataert, E., Arons, J., Metzger, B. D., & Thompson, T. A. 2007, MNRAS, 380, 1541
Bucciantini, N., Quataert, E., Metzger, B. D., et al. 2009, MNRAS, 396, 2038
Burrows, D. N., Hill, J. E., Nousek, J. A., et al. 2005, SSRv, 120, 165
Cano, Z. 2015, GCN, 18552, 1
Cenko, S. B., Fox, D. B., Moon, D.-S., et al. 2006, PASP, 118, 1396
Chandra, P., & Nayana, A. J. 2015a, GCN, 18608, 1
Chandra, P., & Nayana, A. J. 2015b, GCN, 18620, 1
Chen, W., Xie, W., Lei, W.-H., et al. 2017, ApJ, 849, 119
Chevalier, R. A. 1989, ApJ, 346, 847
Chevalier, R. A., & Li, Z.-Y. 2000, ApJ, 536, 195

Chincarini, G., Mao, J., Margutti, R., et al. 2010, MNRAS, 406, 2113
Chincarini, G., Moretti, A., Romano, P., et al. 2007, ApJ, 671, 1903
Dai, Z. G., & Liu, R.-Y. 2012, ApJ, 759, 58
Dai, Z. G., & Lu, T. 1998, A&A, 333, L87
Dai, Z. G., & Wu, X. F. 2003, ApJL, 591, L21
Dermer, C. D. 2004, ApJ, 614, 284
Dermer, C. D., Chiang, J., & Mitman, K. E. 2000, ApJ, 537, 785
Dichiara, S., Kopac, D., Guidorzi, C., Kobayashi, S., & Gomboc, A. 2015, GCN, 18510, 1
Evans, P. A., Willingale, R., Osborne, J. P., et al. 2010, A&A, 519, A102
Falcone, A. D., Morris, D., Racusin, J., et al. 2007, ApJ, 671, 1921
Fan, Y.-Z., Dai, Z.-G., Huang, Y.-F., & Lu, T. 2002, ChJAA, 2, 449
Fan, Y. Z., Wei, D. M., & Wang, C. F. 2004, A&A, 424, 477
Fan, Y.-Z., Yu, Y.-W., Xu, D., et al. 2013, ApJL, 779, L25
Fenimore, E. E., Madras, C. D., & Nayakshin, S. 1996, ApJ, 473, 998
Filippenko, A. V., Li, W. D., Treffers, R. R., & Modjaz, M. 2001, ASPC, 246, 121
Fitzpatrick, E. L. 1999, PASP, 111, 63
Foreman-Mackey, D., Hogg, D. W., Lang, D., & Goodman, J. 2013, PASP, 125, 306
Galama, T. J., Vreeswijk, P. M., van Paradijs, J., et al. 1998, Natur, 395, 670
Gao, H., Lei, W.-H., Zou, Y.-C., Wu, X.-F., & Zhang, B. 2013, NewAR, 57, 141
Gao, H., Wang, X.-G., Mészáros, P., & Zhang, B. 2015, ApJ, 810, 160
Gehrels, N., Chincarini, G., Giommi, P., et al. 2004, ApJ, 611, 1005
Ghisellini, G., Ghirlanda, G., Nava, L., & Firmani, C. 2007, ApJL, 658, L75
Golenetskii, S., Aptekar, R., Frederiks, D., et al. 2015, GCN, 18516, 1
Granot, J., De Colle, F., & Ramirez-Ruiz, E. 2018, MNRAS, 481, 2711
Granot, J., & Kumar, P. 2003, ApJ, 591, 1086
Granot, J., Nakar, E., & Piran, T. 2003, Natur, 426, 138
Granot, J., & Sari, R. 2002, ApJ, 568, 820
Hamidani, H., Sato, Y., Kashiyama, K., et al. 2025, ApJL, 986, L4
Harrison, R., & Kobayashi, S. 2013, ApJ, 772, 101
Hentunen, V. P., Nissinen, M., & Salmi, T. 2015, GCN, 18503, 1
H.E.S.S. Collaboration, Abdalla, H., Aharonian, F., et al. 2021, Sci, 372, 1081
Hjorth, J., & Bloom, J. S. 2012, in Gamma-Ray Bursts, ed. C. Kouveliotou, R. A. M. J. Wijers, & S. Woosley (Cambridge Univ. Press), 169
Hjorth, J., Sollerman, J., Møller, P., et al. 2003, Natur, 423, 847
Hogg, D. W., Bovy, J., & Lang, D. 2010, arXiv:1008.4686
Huang, X.-L., Xin, L.-P., Yi, S.-X., et al. 2016, ApJ, 833, 100
Huang, Y. F., Dai, Z. G., & Lu, T. 1999, MNRAS, 309, 513
Huang, Y. F., Gou, L. J., Dai, Z. G., & Lu, T. 2000, ApJ, 543, 90
Huang, Y. F., Wu, X. F., Dai, Z. G., Ma, H. T., & Lu, T. 2004, ApJ, 605, 300
Japelj, J., Kopač, D., Kobayashi, S., et al. 2014, ApJ, 785, 84
Klebesadel, R. W., Strong, I. B., & Olson, R. A. 1973, ApJL, 182, L85
Kluźniak, W., & Ruderman, M. 1998, ApJL, 505, L113
Kobayashi, S., & Zhang, B. 2003, ApJL, 582, L75
Kong, D.-F., Wang, X.-G., Zheng, W., et al. 2024, ApJ, 971, 56
Kouveliotou, C., Meegan, C. A., Fishman, G. J., et al. 1993, ApJL, 413, L101
Kozlov, V., Andreev, M., Mazaeva, E., et al. 2015, GCN, 18558, 1
Kulkarni, S. R., Frail, D. A., Wieringa, M. H., et al. 1998, Natur, 395, 663
Kumar, P., Narayan, R., & Johnson, J. L. 2008, Sci, 321, 376
Kumar, P., & Panaitescu, A. 2000, ApJL, 541, L51
Kumar, P., & Panaitescu, A. 2003, MNRAS, 346, 905
Kumar, P., & Piran, T. 2000, ApJ, 532, 286
Kumar, P., & Zhang, B. 2015, PhR, 561, 1
Kusafuka, Y., Obayashi, K., Asano, K., & Yamazaki, R. 2025, MNRAS, 544, 3115
Laskar, T., Alexander, K., & Berger, E. 2015, GCN, 18508, 1
Lazzati, D., Perna, R., Morsony, B. J., et al. 2018, PhRvL, 120, 241103
Lazzati, D., Rossi, E., Covino, S., Ghisellini, G., & Malesani, D. 2002, A&A, 396, L5
Lee, H. K., Wijers, R. A. M. J., & Brown, G. E. 2000, PhR, 325, 83
Lei, W.-H., Yuan, Q., Zhang, B., & Wang, D. 2016, ApJ, 816, 20
Lei, W.-H., & Zhang, B. 2011, ApJL, 740, L27
Lei, W.-H., Zhang, B., & Liang, E.-W. 2013, ApJ, 765, 125
LHAASO Collaboration, Cao, Z., Aharonian, F., et al. 2023, Sci, 380, 1390
Li, L., Liang, E.-W., Tang, Q.-W., et al. 2012, ApJ, 758, 27
Li, L., Wu, X.-F., Huang, Y.-F., et al. 2015, ApJ, 805, 13
Li, L.-X. 2000, PhRvD, 61, 084016
Li, W., Filippenko, A. V., Chornock, R., & Jha, S. 2003, PASP, 115, 844
Liang, E.-W., Li, L., Gao, H., et al. 2013, ApJ, 774, 13
Liang, E. W., Zhang, B., O'Brien, P. T., et al. 2006, ApJ, 646, 351
Liang, E.-W., Zhang, B.-B., & Zhang, B. 2007, ApJ, 670, 565
Lin, J., Lu, R.-J., Lin, D.-B., & Wang, X.-G. 2020, ApJ, 895, 46
Lü, H.-J., Lan, L., Zhang, B., et al. 2018a, ApJ, 862, 130
Lü, H.-J., & Zhang, B. 2014, ApJ, 785, 74
Lü, H.-J., Zhang, B., Lei, W.-H., Li, Y., & Lasky, P. D. 2015, ApJ, 805, 89
Lü, H.-J., Zou, L., Lan, L., & Liang, E.-W. 2018b, MNRAS, 480, 4402
MacFadyen, A. I., Woosley, S. E., & Heger, A. 2001, ApJ, 550, 410
MAGIC Collaboration, Acciari, V. A., Ansoldi, S., et al. 2019, Natur, 575, 455
Margutti, R., Guidorzi, C., Chincarini, G., et al. 2010, MNRAS, 406, 2149
Maselli, A., D'Ai, A., Lien, A. Y., et al. 2015, GCN, 18478, 1
McKinney, J. C. 2005, ApJL, 630, L5
Meegan, C., Lichti, G., Bhat, P. N., et al. 2009, ApJ, 702, 791
Meegan, C. A., Fishman, G. J., Wilson, R. B., et al. 1992, Natur, 355, 143
Meszaros, P., & Rees, M. J. 1993, ApJ, 405, 278
Mészáros, P., & Rees, M. J. 1997, ApJ, 476, 232
Mészáros, P., & Rees, M. J. 1999, MNRAS, 306, L39
Metzger, B. D., Giannios, D., Thompson, T. A., Bucciantini, N., & Quataert, E. 2011, MNRAS, 413, 2031
Moskvitin, A. 2015, GCN, 18521, 1
Nagataki, S. 2011, PASJ, 63, 1243
Nakar, E., & Granot, J. 2007, MNRAS, 380, 1744
Nakar, E., & Piran, T. 2004, MNRAS, 353, 647
Nappo, F., Pescalli, A., Oganesyan, G., et al. 2017, A&A, 598, A23
Narayan, R., Piran, T., & Kumar, P. 2001, ApJ, 557, 949
Nedora, V., Crosato Menegazzi, L., Peretti, E., Dietrich, T., & Shibata, M. 2025, MNRAS, 538, 2089
Nicholl, M., Guillochon, J., & Berger, E. 2017, ApJ, 850, 55
Nousek, J. A., Kouveliotou, C., Grupe, D., et al. 2006, ApJ, 642, 389
Oksanen, A. 2015, GCN, 18567, 1
Palmer, D. M., Barthelmy, S. D., Cummings, J. R., et al. 2015, GCN, 18496, 1
Panaitescu, A., Mészáros, P., Gehrels, N., Burrows, D., & Nousek, J. 2006, MNRAS, 366, 1357
Panaitescu, A., Mészáros, P., & Rees, M. J. 1998, ApJ, 503, 314
Pei, Y. C. 1992, ApJ, 395, 130
Perley, D. A., & Cenko, S. B. 2015, GCN, 18481, 1
Perley, D. A., Hillenbrand, L., & Prochaska, J. X. 2015, GCN, 18487, 1
Pian, E., D'Avanzo, P., Benetti, S., et al. 2017, Natur, 551, 67
Popham, R., Woosley, S. E., & Fryer, C. 1999, ApJ, 518, 356
Pozanenko, A., Mazaeva, E., Volnova, A., & Burhonov, O. 2015, GCN, 18635, 1
Primorac, D., Muccino, M., Moradi, R., et al. 2018, ARep, 62, 933
Protsyuk, Y., & Kovalchuk, O. 2015, GCN, 18533, 1
Racusin, J. L., Karpov, S. V., Sokolowski, M., et al. 2008, Natur, 455, 183
Rees, M. J., & Mészáros, P. 1998, ApJL, 496, L1
Ren, J., Lin, D.-B., Zhang, L.-L., et al. 2019, ApJ, 885, 60
Ren, J., Wang, Y., & Dai, Z.-G. 2024, ApJ, 962, 115
Rhoads, J. E. 1997, ApJL, 487, L1
Rhoads, J. E. 1999, ApJ, 525, 737
Roming, P. W. A., Kennedy, T. E., Mason, K. O., et al. 2005, SSRv, 120, 95
Rowlinson, A., O'Brien, P. T., Metzger, B. D., Tanvir, N. R., & Levan, A. J. 2013, MNRAS, 430, 1061
Rowlinson, A., O'Brien, P. T., Tanvir, N. R., et al. 2010, MNRAS, 409, 531
Ruffini, R., Becerra, L., Bianco, C. L., et al. 2018, ApJ, 869, 151
Ryan, G., van Eerten, H., Piro, L., & Troja, E. 2020, ApJ, 896, 166
Sahu, D., & Anupama, G. 2015, GCN, 18609, 1
Sari, R., & Piran, T. 1999, ApJL, 517, L109
Sari, R., Piran, T., & Halpern, J. P. 1999, ApJL, 519, L17
Sari, R., Piran, T., & Narayan, R. 1998, ApJL, 497, L17
Schlafly, E. F., & Finkbeiner, D. P. 2011, ApJ, 737, 103
Soderberg, A. M. 2007, AIPC, 937, 492
Sonbas, E., Guver, T., Gogus, E., et al. 2015, GCN, 18518, 1
Stanek, K. Z., Matheson, T., Garnavich, P. M., et al. 2003, ApJL, 591, L17
Tagliaferri, G., Goad, M., Chincarini, G., et al. 2005, Natur, 436, 985
Tang, C.-H., Huang, Y.-F., Geng, J.-J., & Zhang, Z.-B. 2019, ApJS, 245, 1
Tanvir, N. R., Levan, A. J., González-Fernández, C., et al. 2017, ApJL, 848, L27
Thompson, C. 1994, MNRAS, 270, 480
Tian, X., Lü, H., Tan, W., et al. 2025, ApJ, 982, 19
Toelge, K., Yu, H. F., & Meegan, C. A. 2015, GCN, 18492, 1
Troja, E., Cusumano, G., O'Brien, P. T., et al. 2007, ApJ, 665, 599
Usov, V. V. 1992, Natur, 357, 472
van Eerten, H., van der Horst, A., & MacFadyen, A. 2012, ApJ, 749, 44
Vestrand, W. T., Wozniak, P. R., Wren, J. A., et al. 2005, Natur, 435, 178
Vestrand, W. T., Wren, J. A., Wozniak, P. R., et al. 2006, Natur, 442, 172
Vogt, S. S., Allen, S. L., Bigelow, B. C., et al. 1994, SPIE, 2198, 362
Wang, D. X., Xiao, K., & Lei, W. H. 2002, MNRAS, 335, 655
Wang, H., Dastidar, R. G., Giannios, D., & Duffell, P. C. 2024, ApJS, 273, 17
Wang, S. Q., Wang, L. J., Dai, Z. G., & Wu, X. F. 2015a, ApJ, 799, 107
Wang, S. Q., Wang, L. J., Dai, Z. G., & Wu, X. F. 2015b, ApJ, 807, 147

Wang, X.-G., Chen, Y.-Z., Huang, X.-L., et al. 2022, ApJ, 939, 39
Wang, X.-G., Li, L., Yang, Y.-P., et al. 2020, ApJL, 894, L22
Wang, X.-G., Liang, E.-W., Li, L., et al. 2013, ApJ, 774, 132
Wang, X.-G., Zhang, B., Liang, E.-W., et al. 2015, ApJS, 219, 9
Wang, X.-G., Zhang, B., Liang, E.-W., et al. 2018, ApJ, 859, 160
Wang, X.-G., Zhou, J.-W., Zhou, Z.-M., et al. 2024, ApJ, 969, 146
Wang, Y., Chen, C., & Zhang, B. 2026, JHEAp, 50, 100490
Wiggins, P. 2015, GCN, 18539, 1
Willingale, R., Starling, R. L. C., Beardmore, A. P., Tanvir, N. R., & O'Brien, P. T. 2013, MNRAS, 431, 394
Woosley, S. E. 1993, ApJ, 405, 273
Woosley, S. E., & Bloom, J. S. 2006, ARA&A, 44, 507
Wren, J., Vestrand, W. T., Wozniak, P., & Davis, H. 2015, GCN, 18495, 1
Wu, X.-F., Hou, S.-J., & Lei, W.-H. 2013, ApJL, 767, L36
Xie, L., Wang, X.-G., Zheng, W., et al. 2020, ApJ, 896, 4
Xin, L., Han, X., Li, H., et al. 2023, NatAs, 7, 724
Xin, L. P., Wang, X. F., Wei, J. Y., et al. 2015, GCN, 18515, 1
Xiong, R.-J., Huang, X.-L., & Wang, Z.-R. 2024, ApJL, 966, L25
Xu, D., Zhang, C. M., Cao, C., & Hu, S. M. 2015, GCN, 18485, 1
Yamazaki, R., Toma, K., Ioka, K., & Nakamura, T. 2006, MNRAS, 369, 311
Yang, Z., Lü, H.-J., Yang, X., Shen, J., & Yi, S.-X. 2024, MNRAS, 535, 2482
Yano, Y., Yoshii, T., Saito, Y., et al. 2015, GCN, 18491, 1
Yi, S.-X., Wu, X.-F., & Dai, Z.-G. 2013, ApJ, 776, 120
Yi, S.-X., Wu, X.-F., Zou, Y.-C., & Dai, Z.-G. 2020, ApJ, 895, 94
Yu, Y. B., Wu, X. F., Huang, Y. F., et al. 2015, MNRAS, 446, 3642
Zhang, B. 2018, The Physics of Gamma-Ray Bursts (Cambridge Univ. Press)
Zhang, B., Fan, Y. Z., Dyks, J., et al. 2006, ApJ, 642, 354
Zhang, B., & Kobayashi, S. 2005, ApJ, 628, 315
Zhang, B., Kobayashi, S., & Mészáros, P. 2003, ApJ, 595, 950
Zhang, B., & Mészáros, P. 2001a, ApJL, 552, L35
Zhang, B., & Mészáros, P. 2001b, ApJ, 559, 110
Zhang, B., & Mészáros, P. 2002, ApJ, 566, 712
Zhang, J., Mao, J., & Bai, J. 2015a, GCN, 18513, 1
Zhang, J., Mao, J., & Bai, J. 2015b, GCN, 18493, 1
Zhang, Q., Lei, W. H., Zhang, B. B., et al. 2018, MNRAS, 475, 266
Zhang, S., Jin, Z.-P., & Wei, D.-M. 2015, ApJ, 798, 3
Zhang, W., Woosley, S. E., & Heger, A. 2008, ApJ, 679, 639
Zhao, L., Liu, L., Gao, H., et al. 2020, ApJ, 896, 42
Zheng, J.-H., Zhu, J.-P., Lu, W., & Zhang, B. 2025, ApJ, 985, 21
Zheng, W., & Filippenko, A. V. 2015, GCN, 18479, 1
Zou, L., Zhou, Z.-M., Xie, L., et al. 2019, ApJ, 877, 153
Zou, Y. C., Wu, X. F., & Dai, Z. G. 2005, MNRAS, 363, 93